

AD-A140 378

THREE-DIMENSIONAL LAMINAR SEPARATION(U) VIRGINIA
POLYTECHNIC INST AND STATE UNIV BLACKSBURG DEPT OF E..
D P TELIONIS ET AL. DEC 83 VPI-E-83-48

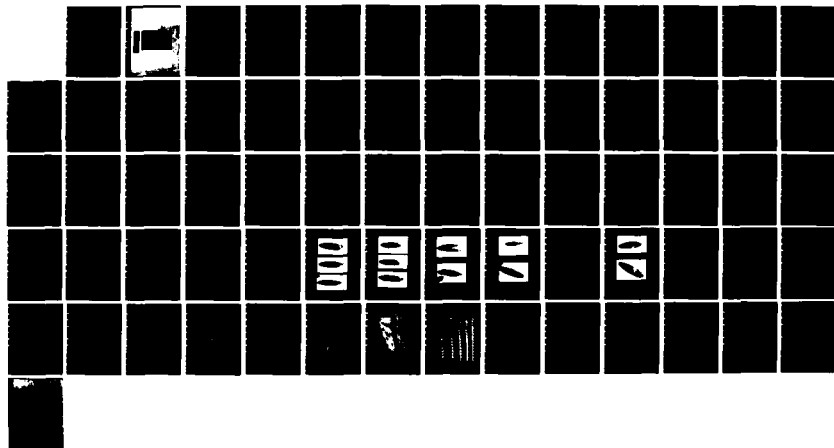
1/1

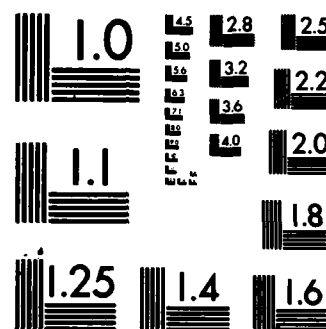
UNCLASSIFIED

DTNSRDC/ASED-CR-04-83 N00167-82-K-0005

F/G 20/4

NL





MICROCOPY RESOLUTION TEST CHART
NATIONAL BUREAU OF STANDARDS-1963-A

THREE-DIMENSIONAL LAMINAR SEPARATION

D. P. Telionis and C. E. Costis
Department of Engineering Science & Mechanics
Virginia Polytechnic Institute & State University

(12)

DTNSRDC-ASED-CR-04-83

THREE-DIMENSIONAL LAMINAR SEPARATION

D. P. Telionis and C. E. Costis
Department of Engineering Science & Mechanics
Virginia Polytechnic Institute & State University

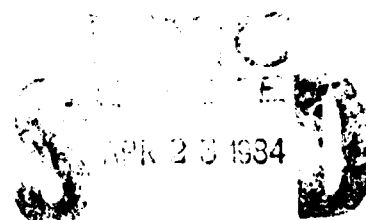
December 1983

Theoretical Phase Report for May 1982 - August 1984

APPROVED FOR PUBLIC RELEASE: DISTRIBUTION UNLIMITED

Prepared for

DAVID W. TAYLOR NAVAL SHIP RESEARCH AND DEVELOPMENT CENTER
Aviation and Surface Effects Department
Bethesda, Maryland 20084



A

REPORT DOCUMENTATION PAGE		READ INSTRUCTIONS BEFORE COMPLETING FORM
1. REPORT NUMBER DTNSRDC/ASED-CR-04-83	2. GOVT ACCESSION NO. AD-A140 378	3. RECIPIENT'S CATALOG NUMBER
4. TITLE (and Subtitle) THREE-DIMENSIONAL LAMINAR SEPARATION		5. TYPE OF REPORT & PERIOD COVERED Final Report
7. AUTHOR(s) Demetri Pyrros Telionis and Christopher Evangelos Costis		6. PERFORMING ORG. REPORT NUMBER VPI-E-83-48
9. PERFORMING ORGANIZATION NAME AND ADDRESS Virginia Polytechnic Institute & State University Blacksburg, Virginia 24061		8. CONTRACT OR GRANT NUMBER(s) N00167-82-K-0085
11. CONTROLLING OFFICE NAME AND ADDRESS David W. Taylor Naval Ship R&D Center Aviation & Surface Effects Dept. Bethesda, Maryland 20084		10. PROGRAM ELEMENT, PROJECT, TASK AREA & WORK UNIT NUMBERS
14. MONITORING AGENCY NAME & ADDRESS (if different from Controlling Office)		12. REPORT DATE October, 1983
		13. NUMBER OF PAGES 67
		15. SECURITY CLASS. (of this report) UNCLASSIFIED
		15a. DECLASSIFICATION/DOWNGRADING SCHEDULE
16. DISTRIBUTION STATEMENT (of this Report) APPROVED FOR PUBLIC RELEASE: DISTRIBUTION UNLIMITED		
17. DISTRIBUTION STATEMENT (of the abstract entered in Block 20, if different from Report)		
18. SUPPLEMENTARY NOTES		
19. KEY WORDS (Continue on reverse side if necessary and identify by block number) Three-Dimensional Boundary Layers Three-Dimensional Separation Three-Dimensional Wakes Skin-Friction Lines		
20. ABSTRACT (Continue on reverse side if necessary and identify by block number) Simple methods for obtaining estimates of skin-friction lines and separation lines are discussed. Results for prolate spheroids and ellipsoids are compared with earlier detailed numerical studies. Flow visualizations of the regions of interest are presented and compared with the calculated results. Streamwise and cross flow velocity profiles measured by Laser Doppler Velocimeter are displayed.		

Table of Contents

	<u>Page</u>
List of Figures	i
Abstract	iv
1. Introduction	1
2. Three Simple Methods of Calculation	4
3. Flow Visualization	14
4. Velocity Measurements	17
5. Conclusions	24
6. Acknowledgment	24
References	25



A1

List of Figures

	<u>Page</u>
Fig. 1 Definition of coordinates for (a) in cylinder in jaw and (b) a prolate spheroid.	27
Fig. 2 Flow about an ellipsoid with axes ratios $a:b:c = 4:1:1$ (prolate spheroid) at an angle of attack $\alpha = 30^\circ$	28
Fig. 3 Flow about an ellipsoid with axes ratios $a:b:c = 70:10:7$ and a free stream $U_\infty = \cos 15^\circ$, $V_\infty = \sin 15^\circ$, $W_\infty = \sin 15^\circ$	29
Fig. 4 Flow about an ellipsoid with axes ratios $a:b:c = 50:30:10$ and free stream $U_\infty = \cos 30^\circ$, $V_\infty = \sin 15^\circ$, $W_\infty = \sin 15^\circ$	30
Fig. 5 Flow about an ellipsoid with axes ratios $a:b:c = 4:1:1$ (prolate spheroid) at an angle of attack $\alpha = 30^\circ$ (surface-streamline integration method).	31
Fig. 6 Lines of separation for a prolate spheroid with axes ratios $a/b = 6$ and angles of attack $\alpha = 5^\circ, 10^\circ$ and 15° . ——, Stock ⁸ ; -----, Geissler ¹⁹ ; □, present method. ..	32
Fig. 7 Lines of separation for a prolate spheroid with axes ratios $a/b = 4$ and angles of attack $\alpha = 15^\circ$ and 30° . ——, Stock ⁸ ; -----, Geissler ¹⁹ ; □, present method. ...	33
Fig. 8 Lines of separation for a prolate spheroid with axes ratios $a/b = 2$ and angle of attack $\alpha = 20^\circ$. ——, Stock ⁸ ; -----, Geissler ¹⁹ ; □, present method.	34
Fig. 9 Lines of separation and external streamlines for a prolate spheroid of $a/b = 6$ at an angle of attack $\alpha = 6^\circ$. ——, Ref. 6; -----, Ref. 3; □, present approximate method.	35
Fig. 10 Lines of separation and external streamlines for a prolate spheroid of $a/b = 6$ at an angle of attack $\alpha = 15^\circ$ as reported in Ref. 6; □, present approximate method; -o-o-o-o, present experimental data.	36
Fig. 11 Lines of separation and external streamlines for a prolate spheroid of $a/b = 4$ at an angle of attack $\alpha = 30^\circ$ as reported in Ref. 6; □, present approximate method; o-o-o-o-o, present experimental data.	37
Fig. 12 Skin friction lines for $\alpha = 3^\circ$. (a) Leeward view, (b) View from $\phi = 120^\circ$, (c) Side view.	38
Fig. 13 Skin friction lines for $\alpha = 6^\circ$. (a) Leeward view, (b) View from $\phi = 120^\circ$, (c) Side view.	39

Fig. 14	Skin friction and inviscid lines for $\alpha = 10^\circ$. (a) Leeward view, (b) View from $\phi = 120^\circ$	40
Fig. 15	Skin friction and inviscid lines for $\alpha = 20^\circ$. (a) Leeward view, (b) View from $\phi = 120^\circ$	41
Fig. 16	The three regions of difficult accessibility for $\alpha = 10^\circ$. (a) Leeward view, (b) View from $\phi = 120^\circ$	42
Fig. 17	Skin friction and inviscid lines for $\alpha = 30^\circ$. (a) Leeward view, (b) View from $\phi = 120^\circ$. For comparison, see flow visualizations of Fig. 14.	43
Fig. 18	Approximate form of skin friction lines for $\alpha = 10^\circ$. (a) Leeward view, (b) View from $\phi = 120^\circ$	44
Fig. 19	Approximate form of skin friction lines for $\alpha = 20^\circ$. (a) Leeward view, (b) View from $\phi = 120^\circ$	45
Fig. 20	Qualitative shape of skin-friction lines super- imposed on a Figure from Ref. 6.	46
Fig. 21	Schematic representation of the crossing of 3 beams. All 3 beams are in the same plane. Interference bet- ween beam 1 and 2 generates the velocity component V_{12} and interference between 2 and 3 generates the component V_{23}	47
Fig. 22	The optical bench for the measurement of 2 components.	48
Fig. 23	Example of laser beam locations with respect to the body and output of program for the calculation of measuring position.	49
Fig. 24	Extension of the idea of Fig. 21, to measure a third velocity components.	50
Fig. 25	RMS spectrum of the velocity fluctuation. If the low frequencies (less than 1 Hz) are eliminated, then the turbulence level is less than 0.1%. The spikes in the spectrum correspond to the 60 Hz and its multiples and are due to the power supply.	51
Fig. 26	The actual experimental points shown together with the smoothed profile on the leeward side at the fourth station.	52
Fig. 27	The u-component velocity profile. Horizontal and vertical scales are marked in tenths of free stream velocity and increments of $1/10''$ (and 0.85 mm) respectively.	53
Fig. 28	The u-component velocity profile calculated by Patel and Baek ²⁰	54

Fig. 29	The u- and v-velocity components at the first station of measurement.	55
Fig. 30	The u- and v-velocity components at the second station of measurement.	56
Fig. 31	The u- and v-velocity components at the third station of measurement.	57
Fig. 32	The u- and v-velocity components at the fourth station of measurement.	58
Fig. 33	The u- and v-velocity components at the fifth station of measurement.	59
Fig. 34	Composite figure showing all the velocity profiles in the two-dimensional space of the ellipsoid surface.	60

Abstract

Simple methods for obtaining estimates of skin-friction lines and separation lines are discussed. Results for prolate spheroids and ellipsoids are compared to earlier detailed numerical studies. Flow visualizations of the regions of interest are presented and compared with the calculated results. Streamwise and cross flow velocity profiles measured by Laser Doppler Velocimeter are displayed.

1. Introduction

The determination of the line of separation over three-dimensional bodies of arbitrary shapes is a difficult problem requiring the solution of the boundary-layer equation or the full Navier-Stokes equations. A good number of careful boundary-layer calculations have been carried out in the past decade for the flow about a prolate spheroid.¹⁻⁵ These calculations have clearly demonstrated that the difficulty of the problem centers mostly about the proper choice of the grid shape. Most recently, further improvements on methods of integration that conform with the principles of influence and dependence have appeared.^{6,7} The difficulties multiply as one approaches the line of separation. Taking into account the errors involved in solving numerically the boundary-layer equations in the vicinity of separation and the fact that these equations are not even valid in this region, the usefulness of such methods becomes questionable. Moreover, their application to more general body shapes is a formidable exercise, requiring the constant attention of experienced investigators.

One of the purposes of the present effort is to provide or expand upon some significantly more simple methods of calculation of the separation line. The first is based on local similarity concepts and permits the estimate of the skin friction distribution as well as the line of separation. The second allows the determination of the separation line by criteria based exclusively on potential flow. This is admittedly a very simplistic point of view, but the accuracy of the results has surprised the authors and certainly deserves to be communicated with the engineering community.

Approximate methods are available, as for example integral methods⁸ or streamline methods.^{9,10} These methods are considerably simpler than the methods based on the complete three-dimensional boundary-layer equations. The new methods proposed here are even simpler and could easily be programmed on a pocket computer to provide a quick and reasonably accurate answer for a complex configuration. However, a more promising approach would be to couple a streamline method^{9,10} with a good local similarity model. In this way the history of the developing boundary layer can be accounted for. In this report a first attempt along this direction is included.

The second part of this report includes some flow visualizations of the same problem. Although earlier experiments have been reported,¹¹⁻¹⁵ this experiment was conducted for Reynolds numbers below 2000, which ensures that the flow is purely laminar and free of any growing instabilities. Comparison of experimental data with the theory are included. However, a careful comparison will require digitizing the flow visualization information. The experimental results offer some very exciting new information on the physical properties of three-dimensional separation and allow the numerical results obtained by others to be re-interpreted.

In the last section of the report, a two- and three-component LDV rig especially designed and constructed for the measurement of three-dimensional boundary layers is described. Experimental data are presented for two-component velocity profiles at several selected stations. These data are compared to boundary layer calculations reported in Ref. 20. It should be emphasized here that to the knowledge of the authors, no other velocity profile measurements over a prolate spheroid at such

low Reynolds numbers have been reported so far. In fact, the only experimental information on velocity distributions on a prolate spheroid pertains to the cross section $x/L = 0.64$ only, as reported in Ref. 14. Detailed information on three-dimensional velocity profiles were obtained by Ramaprian et al.²¹ by 3-hole probes, but on an arbitrarily defined body of revolution. Moreover, both studies^{14,21} were conducted in the turbulent regime. The Laser-Doppler Velocimeter is employed here for the first time to measure three-dimensional boundary-layer profiles.

2. Three Simple Methods of Calculation

In this section we describe three very simple methods for estimating the approximate form of skin friction lines and lines of separation. The first is based on an assumption of local three-dimensional boundary-layer similarity. The second is based on some observations of existing data. Neither of the two requires integration of differential equations, although the first could be expanded to include the history of the boundary layer and integration along a streamline. The third is a refinement of an existing streamline method.

For a few very special three-dimensional configurations it is relatively easy to obtain accurate numerical solutions of the three-dimensional boundary-layer equations. One class of such configurations are cylinders of arbitrary cross section in yaw with respect to the oncoming flow. For these special bodies, referred to here as Sears bodies, the two momentum equations are uncoupled and the solution can be easily obtained.¹⁶ We assume that the flow about a general 3-D configuration is locally similar to the flow about one of the special bodies discussed above. In other words, we assume that the properties of the boundary layer at a specific station on the body of interest are similar to the properties at a suitably chosen point on a Sears body. The criterion for the determination of the point on the special body which corresponds to the point of our interest is based on properties of the outer flow. The known special solution is thus considered essentially a bank of properties which are drawn according to certain rules, in order to synthesize the properties of the flow about the body of interest. One of the physical and mathematical properties of the boundary layer which is missing from such a model is history. However, the limitations are

not so severe if there are no sharp changes in the pressure gradient distribution.

Consider the flow about a cylinder in yaw. Let the x , y and z axes be parallel to the generators, along the contour of the body but perpendicular to the generators, and normal to the body, respectively (see Fig. 1a). Let u , v and w be the corresponding velocity components, while U and V are the corresponding outer flow velocity components and U_∞ , V_∞ are the components of the undisturbed free stream, respectively. The governing equations in their dimensionless stretched form then read

$$\frac{\partial v}{\partial y} + \frac{\partial w}{\partial z} = 0 \quad (1)$$

$$v \frac{\partial u}{\partial y} + w \frac{\partial u}{\partial z} = \frac{\partial^2 u}{\partial z^2} \quad (2)$$

$$v \frac{\partial v}{\partial y} + w \frac{\partial v}{\partial z} = v \frac{dv}{dy} + \frac{\partial^2 v}{\partial z^2} \quad (3)$$

In these equations the quantities w and z contain the stretching factor, namely, the square root of the Reynolds number. Notice that there is no pressure gradient term in Eq. (2). Moreover, Eqs. (1) and (3) can be solved independently of Eq. (2). The familiar boundary conditions are

$$u = v = w = 0 \quad \text{at } z = 0 \quad (4)$$

$$u \rightarrow U, \quad v \rightarrow V \quad \text{as } z \rightarrow \infty \quad (5)$$

Solutions to this problem were obtained by Sears¹⁶ for an outer flow given by

$$U = U_{\infty} \quad (6)$$

$$V = C_1 y + C_3 y^3 \quad (7)$$

The solution was obtained in the form of expansions

$$u = U_{\infty} [g_0(z) + \frac{C_3}{C_1} y^2 g_2(z)] \quad (8)$$

$$v = C_1 y f_1(z) + C_3 y^3 f_3(z) \quad (9)$$

and the functions f_1 , f_3 , g_0 and g_2 were tabulated.

The rules of correspondence between points on the body of interest and a Sears body are the following:

- a. The distances s along inviscid streamlines scaled with the total length of each streamline are matched,
- b. the U velocity component is matched,
- c. the V velocity component is matched, and
- d. the velocity gradient along the inviscid streamline is matched.

For a coordinate system x, ϕ defined on a prolate spheroid as shown in Fig. 1b, the four conditions read

$$x = x_s \quad (10)$$

$$v(x, \phi) = C_1 x_s + C_3 x_s^3 \quad (11)$$

$$u(x, \phi) = V \quad (12)$$

$$\frac{\partial (u^2 + v^2)}{\partial s} = C_1 + 3C_3 x_s^2 \quad (13)$$

where x_s is the reduced distance along the Sears body.

Equations (10)-(13) are used to define a Sears body and determine a point on this body. The solution at this point is then given by Eqs. (8) and (9) and is assumed to hold at the corresponding point on the body of interest.

The potential flow about a prolate spheroid at an angle of attack is known in a closed form solution⁹.

$$\frac{u}{V_{\infty}} = \frac{1}{[1 - e^2 (\frac{\lambda}{a} - 1)^2]^{1/2}} \{ (1 + k_a)(\cos \alpha) \cdot [2 \frac{\lambda}{a} - (\frac{\lambda}{a})^2]^{1/2} + (\frac{b}{a})(1 - k_c)(\sin \alpha)(\frac{\lambda}{a} - 1)\cos \phi \} \quad (14)$$

$$\frac{v}{V_{\infty}} = (1 + k_c)\sin \alpha \sin \phi \quad (15)$$

where e is the eccentricity

$$e = \sqrt{1 - (b/a)^2} \quad (16)$$

and k_a and k_c are the following parameters

$$k_a = (\frac{1}{2e} \ln \frac{1+e}{1-e} - 1) / (\frac{1}{1-e^2} - \frac{1}{2e} \ln \frac{1+e}{1-e}) \quad (17)$$

$$k_c = \frac{1}{1 + 2k_a} \quad (18)$$

The same method was employed for the calculation of the viscous flow over an ellipsoid with arbitrary axes a, b, c . In terms of coordinates X, Y and Z aligned with the three major axes a, b and c of the ellipsoid, the potential velocity on the surface of the body can be calculated¹⁷ in terms of an ellipsoid coordinate λ which is constant on all confocal ellipsoids and zero on the ellipsoid of interest. The solution is given in terms of three integrals

$$I_1 = \int_0^{\infty} \frac{d\lambda}{(a^2 + \lambda)\Delta}, \quad I_2 = \int_0^{\infty} \frac{d\lambda}{(b^2 + \lambda)\Delta}, \quad I_3 = \int_0^{\infty} \frac{d\lambda}{(c^2 + \lambda)\Delta} \quad (19)$$

with

$$\Delta^2 = (a^2 + \lambda)(b^2 + \lambda)(c^2 + \lambda) \quad (20)$$

The constants α_0, β_0 and γ_0 and A, B and C are also defined as follows

$$\alpha_0 = abcI_1, \quad A = \frac{2}{2 - \alpha_0} \quad (21)$$

$$\beta_0 = abcI_2, \quad B = \frac{2}{2 - \beta_0} \quad (22)$$

$$\gamma_0 = abcI_3, \quad C = \frac{2}{2 - \gamma_0} \quad (23)$$

The velocity on the body surface is then given in terms of the components of the oncoming stream, $(U_{\infty}, V_{\infty}, W_{\infty})$ and the unit vector normal to the ellipsoid at the point of interest \bar{n} with components (l, m, n)

$$\bar{q} = (AU_{\infty}, BV_{\infty}, CW_{\infty}) - (AU_{\infty}l + BV_{\infty}m + CW_{\infty}n)\bar{n} \quad (24)$$

The unit vector, \bar{n} , normal to the ellipsoid at the point X, Y, Z has the cartesian components

$$l = xa^{-2} \left(\frac{x^2}{a^4} + \frac{y^2}{b^4} + \frac{z^2}{c^4} \right)^{-1/2} \quad (25)$$

$$m = yb^{-2} \left(\frac{x^2}{a^4} + \frac{y^2}{b^4} + \frac{z^2}{c^4} \right)^{-1/2} \quad (26)$$

$$n = zc^{-2} \left(\frac{x^2}{a^4} + \frac{y^2}{b^4} + \frac{z^2}{c^4} \right)^{-1/2} \quad (27)$$

In terms of the quantities, the cartesian components U, V, W of the velocity \bar{q} (see Fig. 1 for notation) are given by

$$U = AU_{\infty} - (AU_{\infty}l^2 + BV_{\infty}ml + CW_{\infty}nl) \quad (28)$$

$$V = BV_{\infty} - (AU_{\infty} \lambda m + BV_{\infty} m^2 + CW_{\infty} nm) \quad (29)$$

$$W = CW_{\infty} - (AU_{\infty} \lambda n + BV_{\infty} mn + CW_{\infty} n^2) \quad (30)$$

To obtain the components u, v and w along the system x, ϕ, z , one needs, of course, to go through the proper transformation.

A computer program was prepared for the calculation of viscous and inviscid streamlines. Marching was started at points equally spaced on a meridional line and was marched in both the upstream and the downstream direction. In this way difficulties encountered in the neighborhood of stagnation points were avoided. In fact, the method provides a clear indication of accuracy at stagnation points where it was demonstrated that all lines pass within a distance of $a/1000$ of each other.

Sample results are shown in Figs. 2, 3 and 4 for a prolate spheroid and an ellipsoid, respectively. In these figures are plotted the projection of lines on planes that correspond to leeward views and side views. The lines that are behind the body are shown dotted. In all figures, envelopes of skin friction lines are clearly developed, thus defining the line of separation. The separation lines found are compatible with analytical predictions of open separation;³ however, the present method is very crude for offering verification of the existence of open or closed separation. Comparison of the relative performance of this method with other methods will be presented later in this report, together with the second method of separation estimates.

A more correct approach, which includes the history of a developing boundary layer, is based on equations along the viscous streamlines^{9,10}

$$\frac{D\theta}{Ds} = \frac{1}{\rho q} \left[\left(\frac{\partial p}{\partial x} - \frac{\partial \tau_x}{\partial z} \right) \sin \theta - \left(\frac{1}{f} \frac{\partial p}{\partial \phi} - \frac{\partial \tau_\phi}{\partial z} \right) \cos \theta \right] - \frac{1}{f} \frac{df}{dx} \sin \theta \quad (31)$$

$$\frac{D\phi}{Ds} = \frac{\sin\theta}{f} \quad (32)$$

$$\frac{Dx}{Ds} = \cos\theta \quad (33)$$

Here θ is the slope of the streamline with respect to the meridional line, s is the distance along the streamline, τ_x and τ_ϕ are the shear stress components along the x and the ϕ direction, respectively; q is the magnitude of the velocity, and f is the radius of the body at the location under consideration.

This system of equations can be integrated along a viscous streamline, at a certain elevation from the wall, provided that an appropriate model for the shear stresses is available.^{9,10} The shape of viscous streamlines can thus be determined. It would be desirable to integrate on the wall in order to obtain the skin friction lines. Unfortunately, the right-hand side of Eq. (31) becomes indeterminate at $z=0$, since both the numerator and the denominator tend to zero. To circumvent this difficulty, a comparison was made with a locally similar flow along a Sears body at each point of the numerical integration. In effect then, with a known $D\phi/Ds$ along the Sears body and stress gradients taken from the Sears body, integration was allowed to proceed from the stagnation point.

More specifically, the same local similarity criteria were employed to define a point on a Sears body. The right-hand side of Eq. (31) and the pressure gradients were then calculated. Moreover, from the exact solution of the Sears problem a relationship between $\partial\tau_x/\partial z$ and $\partial\tau_\phi/\partial z$ was found.

$$\frac{\partial\tau_x}{\partial z} = U_\infty \left[g'_0(z) + \frac{C_3}{C_1} y^2 g'_2(z) \right] \quad (34)$$

$$\frac{\partial \tau_y}{dz} = C_1 y f_1'(z) + C_3 y^3 f_3'(z) \quad (35)$$

These two equations were then solved for the stress gradients assuming a constant small value for the quantity $p q^2$ in the denominator of Eq. (31). The stress gradients were then used in the integration of Eq. (31) over the prolate spheroid, assuming the same small value for the quantity $p q^2$. It was found that the results were not sensitive to the particular value of $p q^2$. Results obtained with this method are plotted in Fig. 5. It is now interesting to observe that the skin friction lines converge to an envelope on both sides of the line of open separation.

Yet another method was discovered by one of us (C.C.) who made the observation that on all problems considered by a variety of methods the inviscid velocity is constant along the line of separation to within an accuracy of a few percent. This value can be estimated from a Sears solution, although a more accurate value could be obtained by a more accurate interactive method. For a unit oncoming flow, the potential velocity on a Sears body takes the value $3.717 \sin^2 \alpha + \cos^2 \alpha$, where α is the yaw angle. Searching for the locus of points where the potential velocity takes this value on a prolate spheroid one falls to within 3% of the separation line calculated by sophisticated methods. To improve on this idea, it was attempted to include a correction term:

$$V_{\text{sep}}^2 = 3.717 \sin^2 \alpha + \cos^2 \alpha + f\left(\frac{a}{b}, \alpha\right) \quad (36)$$

where f may depend on the axes ratio and the yaw angle.

A good choice for the function f can be made by considering the limiting values of α and a/b . Clearly for $\alpha = 0^\circ$ and $\alpha = 90^\circ$ the problem becomes truly axisymmetric and truly two-dimensional, respectively.

A reasonable value for $\alpha = 0$ is the velocity at separation over a sphere¹⁸: $V_{sep}^2 = (\frac{3}{2} \sin 109.6)^2 = 1.9968$ and thus by comparison to Eq. (28), $f(1,0) = (\frac{3}{2})^2 \sin^2(41.72) = 0.99647$. A reasonable assumption for f then could be

$$f(\frac{a}{b}, \alpha) = (\frac{3}{2})^2 \frac{\sin^2(41.72 - \alpha)}{g(a/b)} \quad (37)$$

The function g should have the following limits

$$g(a/b) \rightarrow \infty \text{ as } a/b \rightarrow \infty$$

$$g(a/b) \rightarrow 1 \text{ as } a/b \rightarrow 1$$

since $a/b = 1$ and $a/b = \infty$ correspond to a sphere and an infinite cylinder, respectively. A comparison with detailed earlier calculations for prolate spheroids indicates that for values of a/b equal to 1, 4 and 6, the function $g(a/b)$ should take the values 0.89, 3.78 and 8.75, respectively. A function that would fit through such data is

$$g(a/b) = 0.1031(a/b)^{2.43} + 0.7869 \quad (38)$$

Formula (36) with f and g given by Eqs. (37) and (38) was used to obtain separation lines on prolate spheroids. The results of this method and the method of local similarity described earlier were compared against results obtained by other methods. Results for axes ratios of $a/b = 2, 4$ and 6 and various angles of attack are plotted in Figs. 6, 7 and 8, respectively. The agreement of the present crude method with the methods of Stock⁸ and Geissler¹⁹ is surprisingly good.

Comparison with the work of Refs. 3 and 6 is given in Figs. 9, 10 and 11. In Figs. 10 and 11 our estimates of the separation line as obtained from our flow visualizations are also included. For $\alpha = 6^\circ$ no experimental data is available. However, for $\alpha = 5^\circ$, as will be discussed later, there is no experimental evidence of closed separation.

The separation line should not be continued towards the leeward aft side beyond the Ok which Cebeci, et al.⁶ have identified.

3. Flow Visualization

Experiments were conducted on a prolate spheroid model with axes ratio $b/a = 1/4$. The model was machined out of aluminum and was mounted by a strut from the one end. Dye ports were drilled at strategically chosen points. Colored dyes were supplied by small flexible hoses which were fed and controlled by hypodermic needles. A novel method was introduced in the present studies. Thin hypodermic needles were mounted on the skin of the body, allowing the dyes to be released at the edge of the boundary layer. In this way, skin friction lines and inviscid streamlines emanating from the same station in space could be compared. The tests were conducted in a water tunnel, and still color photographs were taken from views corresponding to inclinations $\phi = 0^\circ, 90^\circ, 120^\circ$ and 180° . These correspond to windward, side, oblique and leeward views, respectively.

Experiments were conducted for angles of attack $\alpha = 3^\circ, 6^\circ, 10^\circ, 15^\circ, 20^\circ$ and 30° . The results confirmed the fact that for very low and very high angles of attack, here for $\alpha = 3^\circ$ and for $\alpha > 30^\circ$, the line of separation is closed around the body. In this case, two critical points can be identified on the line of separation and the general pattern fits nicely one of the models described by Maskell (see discussion in Ref. 3), namely the bubble model. This in the more common terminology is the case of closed separation.

In Figs. 12-15 we display flow visualizations of different views of the flow about a prolate spheroid at angles of attack of $3^\circ, 6^\circ, 10^\circ$ and 20° , respectively. In Fig. 12, a well-behaved closed separation pattern is identified in agreement with all analytical predictions.

For angles of attack $6^\circ < \alpha < 30^\circ$ the evidence clearly indicates that there are two lines of open separation. However, details of the flow uncovered for the first time here shed light to controversial interpretations of earlier numerical results. For this range of angles of attack, it appears that the basic skin-friction line pattern is qualitatively the same. Three distinct regions difficult to be accessed by the free stream become quickly apparent and may be erroneously interpreted as regions of separated flow. The first region is covering the lee side and appears dark in the top view of Fig. 14. It should be emphasized that all the darkened area in this figure is due to dye that has been emitted at only one port in the front part of the model. In the same figure the two lighted areas on the two sides in the aft of the body are strongly suggesting the existence of two separated regions. The pattern could be sketched approximately as in Fig. 16. The two side lobes would then appear to have the shape described by Cebeci et al⁶. What has been known for a long time is that, in fact, the flow remains attached on the leeward plane of symmetry and in its neighborhood. This is corroborated by the fact that the dye stays on the wall until it reaches the small mount at the aft of the body. However, our evidence indicates that what appear as side-separation lobes are actually regions of incredibly large cross flows. This is shown more clearly in Fig. 17. In this figure the inviscid streamlines as well are marked by dyes released at the edge of the boundary layer.

A very large number of flow visualizations obtained point very clearly to a pattern of viscous streamlines shown in Figs. 18 and 19 for $\alpha = 10^\circ$ and 20° , respectively. These patterns have been drawn carefully by an artist who traced the edges of the dye lines from a large

number of flow visualizations. We are presently in the process of using a pattern-recognition computer technique to store all this information in digital form and eventually plot the equivalent of Figs. 18 and 19 by purely mechanical means.

Our evidence as shown in Figs. 13, 14, 15 and the interpretations shown in Figs. 18 and 19 indicates that for these angles of attack, the separation line is of the open type. In fact, the dyes lift off from the body only along the envelope of the skin friction line. This has been observed by the present investigators, but so far it appeared difficult to photograph except in Fig. 17. However, the inviscid streamlines of Figs. 15 and 17 also indicate that the inviscid streamline in the neighborhood of the separation line lift off by a rather large angle with respect to the body.

In view of this evidence, we feel that Cebeci et al⁶ simply reached or rather came very close to the point of zero axial shear stress when they were forced to abandon their integration on the leeside of the body. This possibility was already identified in their presentation. Apparently, the locus of such points may be impossible to pass over with conventional numerical schemes or, in the terminology of Ref. 6, such flows are incalculable. Evidence from the flow visualizations presented here as well as the very large number of data which are not included, indicate that in this region the crossflow angles may reach values of the order of 150° . It is our strong conviction that in the case studied in Ref. 6, the skin-friction lines have the qualitative pattern shown in Fig. 20.

4. Velocity Measurements

In this section we describe a method of measuring velocity profiles in three-dimensional boundary layers. It is emphasized here once more, that to the knowledge of the present authors, Laser-Doppler Velocimetry has not yet been used in measuring three-dimensional flows. Moreover, with the exception of Meier's group,¹²⁻¹⁵ who measured velocities with 3-hole probes, no one has measured velocity profiles on a prolate spheroid. The present results should therefore provide useful information to analyticians who encounter great difficulties in the lee side of a prolate at an angle of attack.^{6,7,8}

A special Laser-Doppler Velocimeter was designed and constructed for the present project. The basic consideration for such a design is that at least two components of velocity are needed in three-dimensional-boundary layers to generate information in the streamwise and the crossflow direction. Moreover, these components must be parallel to the plane tangent to the body surface at the point of interest. It is also necessary that the measuring volume be allowed to approach the wall without blockage of any of the beams by the model. To meet these requirements, three laser beams were generated in the same plane, as shown in Fig. 21. With proper polarization of these beams it is possible to receive scattering signals from interference of beams 1 and 2, and 2 and 3. In this way the components of the velocity in the directions of the bisectors can be obtained. A computer program then allows the determination of Cartesian components.

A special optical bench was constructed. The bench was mounted on traversing towers which permit rotation about the optical axis of the LDV as well as translation in the horizontal and vertical direction as

shown in Fig. 22. The train of sending optics consists of two beam splitters. The first is combined with a polarization rotator to allow control of the power of the two beams. Bragg cells may be used and, in fact, will be necessary to allow measurements in regions of reversing flows. The beams are then all brought in one plane. The outer two beams are displaced outward and then turned back to meet at the measuring volume.

A key feature of the present system is that traversing is permitted perpendicular to the local tangent plane to the body. This is the natural boundary layer coordinate, normal to the surface of the body. Moreover, the two components parallel to the wall surface can be measured all the way down to the wall. This is possible because all three beams are in one plane. A stepping motor has been connected to allow accurate traversing across the boundary layer.

A crucial step in Laser-Doppler measurements is the determination of the location of the measuring volume. In the present experiments this was accomplished as follows. The location of the model in the test section was first determined optically by virtue of a telescope. The space coordinates of the two points of the spheroid surface along its axis of symmetry were recorded. The optical bench was then displaced and rotated until the plane of the beams became tangent to the model and the point of the beam intersection was brought as close as possible to the model surface. The locations of the intersections of the three beams with the two side walls of the tunnel were then determined and stored. A computer program was prepared to estimate the location of the measuring volume on the model by reconstructing the model and the beams. An example of this geometry is shown in Fig. 23. The method allows the

operator to position the system as close as possible to the desired point. The final position of the measuring volume on the model is then recorded. Traversing across the boundary layer is performed perpendicular to the model body in steps controlled by the stepping motor.

It was estimated that the error of positioning the measuring volume on the body in circumferential or axial location should be less than 1% of the length of the model. Errors in vertical displacements should be less than 0.1% of the average thickness of the boundary layer. It should be emphasized that the actual location of the wall, namely the origin of the z-axis was determined by extrapolation after all the data were obtained.

A third channel consisting of a second laser, beam splitter, collecting and receiving optics has been added to the system for measurement of the third component of the velocity. Four beams thus converge at the measuring volume as shown in Fig. 24. These are not orthogonal to each other, but Cartesian components can be calculated on line by the laboratory computer, in terms of the angles shown in the figure.

An automatic system has been designed and tested for collecting and storing all three components for as many points in the boundary layer as necessary. This method has been tested, but only two components were obtained and reported here. With speeds as low as 3 to 10 cm/sec, it was possible to generate boundary layers with thicknesses of a few millimeters on a model 17 cm long. We were able to obtain 40 to 50 data points in such boundary layers, but 600 or 700 points can be easily obtained by cutting the traversing step.

The experimental setup has been arranged and tested together with the data acquisition system on a small water tunnel which did not have

good flow quality. It was planned to move the entire experimental rig and reassemble it around the ESM water tunnel for obtaining the experimental data as described in the proposal. Unfortunately, a sequence of serious problems has set back the work in our laboratory. It was then decided to invest time and effort in improving the quality of the flow in the small tunnel in order to complete the work on this project within the allotted time. A large number of configurations involving combinations of honeycombs and screens has been tested. In Fig. 25 we show the frequency spectrum of the velocity RMS signal. We were very successful in reducing drastically the turbulence level across the entire scale, except for the smallest frequencies. Apparently, a very low frequency is unavoidable and is due to the finite number of blades of the impeller. We then replaced the driving system by a centrifugal pump and installed a number of foam barriers to reduce the head and eliminate the large scale vortices. With this design we were able to lower the overall turbulence level to approximately 0.35%.

The heart of the data acquisition system was a very inexpensive time switch. This was dictated by the large power requirements of solenoids that control blinders of the laser beams. Measurements were obtained sequentially as follows. A blinder blocked beam 1 and therefore the component V_{23} (see Fig. 21) could be measured. The time switch sent a message to the computer to obtain a measurement. Beam 3 was then blocked, and the computer was signaled to measure and store the value of the component V_{12} . A third signal from the time switch to the computer led the program to send pulses to the stepping motor. The number of pulses is preprogrammed to allow fine steps near the wall.

Laser beam 2, the optical axis of symmetry of the Laser Velocimeter was always perpendicular to the direction of the free stream. However, this axis was perpendicular to the ellipsoid axis for only one position of the ellipsoid. This is because the model was inclined with respect to the free stream by the angle of attack, α , but was rotated about an axis parallel to the free stream to expose all surfaces from the windward to the leeward side to the LDV beams. As a result, to obtain velocity components, it was necessary to measure the angle ϕ between the x-axis and the axis of the LDV system as shown in Fig. 21. The velocity components u and v (see Fig. 1 for definition) are then given in terms of the measured quantities and the angles defined in Fig. 21 by virtue of the following straightforward relationships:

$$V_{12} = u \cos\theta_{12} + v \sin\theta_{12} \quad (38)$$

$$V_{23} = u \cos\theta_{13} + v \sin\theta_{13} \quad (39)$$

Errors in the magnitude of the velocity on the order of 0.5% of the mean may be anticipated. However, a simple analysis indicates that for an included angle of $\phi = 6^\circ$ (see Fig. 21), the error anticipated in the circumferential direction may be up to 5% of the mean axial velocity. Considering the fact that the velocity component in this direction may be rather low, this error is sometimes considerable. Clearly a larger angle ϕ should be used in future experiments.

A standard cubic-spline smoothing routine was employed to generate velocity profiles from the discrete experiment data. Comparison of the smoothed profiles and actual experimental data are shown in Fig. 26. In this figure it is also apparent that some data are missing in the immediate vicinity of the wall. The inability to obtain data in this region was attributed to the fact that the size of the measuring volume

was not very small compared to the thickness of the boundary layer. The situation is more critical for axial stations near the nose where the thickness of the boundary layer is very small. In such regions up to 10% of the velocity profile are void of experimental data. The problem can be remedied by using smaller-size pinholes in the photomultipliers.

Data were obtained in this way at five axial stations and five circumferential directions. To facilitate comparison with the numerical results of Ref. 20, the present experimental results are presented in an outlay similar to the one included in this reference. The present experimental results and the numerical results of Patel & Baek²⁰ are shown in Figs. 27 and 28, respectively. It should be noticed that the position of the experimental profiles does not coincide with integral values of coordinates. This is due to difficulties encountered in positioning the measuring volume on the surface of the model. The origin of the velocity profile in this figure is positioned at the point in the $x-\phi$ plane with the coordinates of the $z=0$ position of the measuring volume.

Patel and Baek²⁰ found very abrupt changes in the thickness of the boundary layer and the shape of the velocity profile in the neighborhood of the line of separation, namely, between the angles $\theta = 130^\circ$ and 135° . The velocity profile in the region beyond separation shows clear indications of an inflectional shape. This agrees at least qualitatively with our experimental data. Indeed, the first inflectional profile appears at $\phi \approx 130^\circ$ but not until $x/a = 0.4$. However, the abrupt change of the thickness of the boundary layer is not present. Apparently, the boundary layer equations are an insufficient model for describing exactly the

physical situation in the neighborhood of separation much like the two-dimensional case.

The careful numerical calculations of Patel and Baek²⁰ indicate in the forward half of the body thicker boundary layers closer to the windward side than the experiments. Indeed, the same trend is indicated by the calculations of Cebeci et al,⁶ as shown in Figs. 9 and 10. However, this pattern is reversed for the aft portion of the body.

Both components of the velocity in the axial and circumferential direction are plotted in Figs. 29-32 for four axial stations along the model. The reader is cautioned to the fact that in these figures five different scales of measurement are being employed. The position x, ϕ of the point on the ellipsoid where the data were obtained is the origin of the profile axis. The detailed markings on the orthogonal system shown in each figure provide the velocity scales and the scale in the vertical axis. The two velocity scales parallel to the x and ϕ directions, respectively, should not be confused with the corresponding length scales in these directions. Both velocity scales are marked in tenths of the free stream velocity, whereas the unit length in the z axis corresponds to 1/10 in. or 0.85 mm.

Finally, a collection of all the experimental data obtained is presented in a three-dimensional outlay in Fig. 33. This figure is a composite of Figs. 29-32 and, therefore, the scales are identical to those employed previously.

5. Conclusions

The analytical methods presented here have been proven to provide remarkable accuracy with a minimum of computer time and space. The experimental results, on the other hand, seem to reconcile the points of view of analyticians about closed and open separation. It appears that for a good range of angles of attack there exists open separation which is, in fact, compatible with boundary-layer studies. The present work generated a large number of flow visualizations which conclusively prove this point.

The LDV measurements were obtained at the five stations in the forward portion of the ellipsoid. However, it appears necessary to obtain more data further downstream and, in fact, more detail is necessary in the neighborhood of the origin of open separation.

The work described here is the result of one year's work according to the plan described in our contract with the Navy. However, the findings clearly indicate the need for more work to combine and interpret correctly flow visualizations and LDV measurements in the areas of great interest.

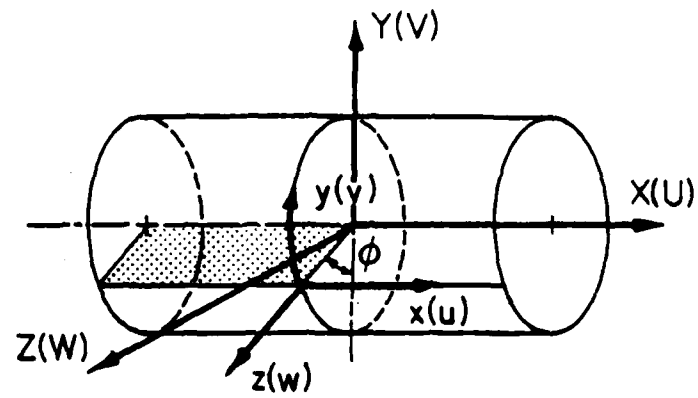
6. Acknowledgment

The support of the Naval Air Systems Command (310-D) under contract No. N00167-82-K-0085 is greatly appreciated. The authors are also indebted to the monitor of the work, Dr. T. C. Tai (DTNSRDC-1606), for his personal and continuous encouragement and his valuable technical assistance.

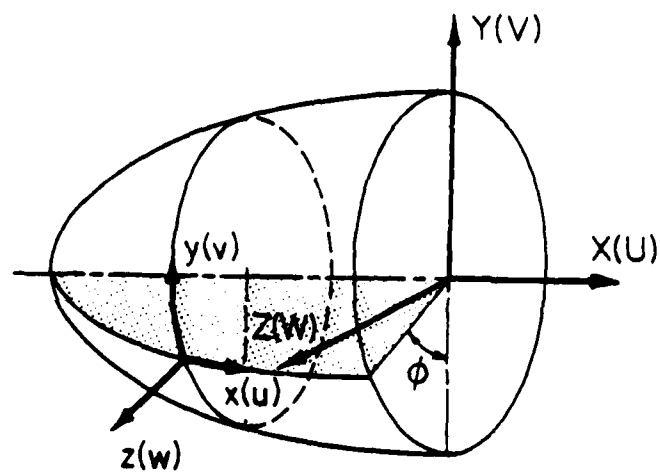
References

1. Blottner, F. G., and Ellis, M. A., "Finite-difference solution of the incompressible three-dimensional boundary-layer equations for a blunt body", Computers & Fluids, Vol. 1, pp. 133-158, 1973.
2. Geissler, W., "Three-dimensional laminar boundary layer over a body of revolution at incidence and with separation", AIAA J., Tech. Note, Vol. 12, No. 12, pp. 1743-1745, 1974.
3. Wang, K. C., "Boundary layer over a blunt body at low incidence with circumferential reversed flow", J. Fluid Mech., Vol. 72, part 1, pp. 49-65, 1975.
4. Hall, M. G., "A numerical method for calculating steady three-dimensional laminar boundary layers", RAE TR G7145, 1967.
5. Patel, V. C., and Choi, D. H., "Calculation of three-dimensional laminar and turbulent boundary layers on bodies of revolution at incidence", 2nd Symposium on Turbulent Shear Flows, pp. 15.14-15.24, Imperial College, London, 1979.
6. Cebeci, T., Khattab, A. K., and Stewartson, K., "Three-dimensional laminar boundary layers and the OK of accessibility", J. Fluid Mech., Vol. 107, pp. 57-87, 1981.
7. Ragab, S. A., "A method for the calculation of three-dimensional boundary layers with circumferential reversed flow on bodies", AIAA-82-1023, 1982.
8. Stock, H. W., "Computation of the boundary layer and separation lines on inclined ellipsoids and of separated flows on infinite swept wings", AIAA-80-1442, 1980.
9. Tai, T. C., "Determination of three-dimensional flow separation by a streamline method", AIAA J., Vol. 19, No. 10, Oct. 1981, pp 1264-1271.
10. Tai, T. C., "Effect of cross flow on the vortex-layer-type 3-dimensional flow separation", in Three-Dimensional Turbulent Boundary Layers, eds. H. H. Fernholz and E. Krause, pp. 117-125, 1982.
11. Han, T. and Patel, V. C., "Flow separation on a spheroid at incidence", J. Fluid Mech., Vol. 92, Part 4, pp. 643-657, 1979.
12. Kreplin, H.-P., Volmers, H., and Meier, H. V., "Experimental determination of wall shear stress vector on an inclined prolate spheroid", AFFDL-TR-80-3088, 1980.
13. Meier, H. U., and Kreplin, H.-P., "Experimental investigation of the transition and separation phenomena on a body of revolution", Z. Flugwiss. Weltraumforsch. 4, Heft2, pp. 65-71, 1980.

14. Meier, H. U., and Kreplin, H.-P., "Experimental study of boundary layer velocity profiles on a prolate spheroid at low incidence in the cross section $x/L = 0.64$ ", AFFDL-TR-80-3088, pp. 169-189, 1980.
15. Meier, H. U., Kreplin, H.-P., and Vollmers, H., "Velocity distributions in 3-D boundary layers and vortex flows developing on an inclined prolate spheroid", DFVLR-AVA-REPORT IB 222 81 CP 1, 1981.
16. Sears, W. R., "The boundary layers of yawed cylinders", J. Aero. Sci., Vol. 15, pp. 49-52, 1942.
17. Band, E. G. U. and Payne, P. R., "The Pressure Distribution on the Surface of an Ellipsoid in Inviscid Flow", Aeronautical Quarterly, pp. 70-84, February 1979.
18. N. Frössling, Verdunstung, Wärmeübergang und Geschwindigkeitsverteilung bei zwei-dimensionalen und rotationssymmetrischen laminaren, Grenzschichtströmungen. Lunds. Univ. Arsskr. N.F. Avd. 2, 35, No. 4, 1940.
19. Geissler, W., "Berechnung der laminaren Ablösung an unsymmetrisch umströmten Rotationskörpern mittels Differenzenverfahren", DFVLR-IB, pp. 251-273, A-31, 1973.
20. Patel, V. C. and Baek, J. H., "Calculation of boundary layers and separation on a spheroid at incidence", in Numerical & Physical Aspects of Aerodynamic Flows, ed., T. Cebeci, Cal. State University, 1983.
21. Ramaprian, B. R., Patel, V. C. and Choi, D. H., "Mean-flow measurements in the three-dimensional boundary layer over a body of revolution at incidence", J. Fluid Mech., Vol. 103, pp. 479-504, 1981.



(a)



(b)

Fig. 1 Definition of coordinates for (a) a cylinder in yaw and (b) a prolate spheroid.

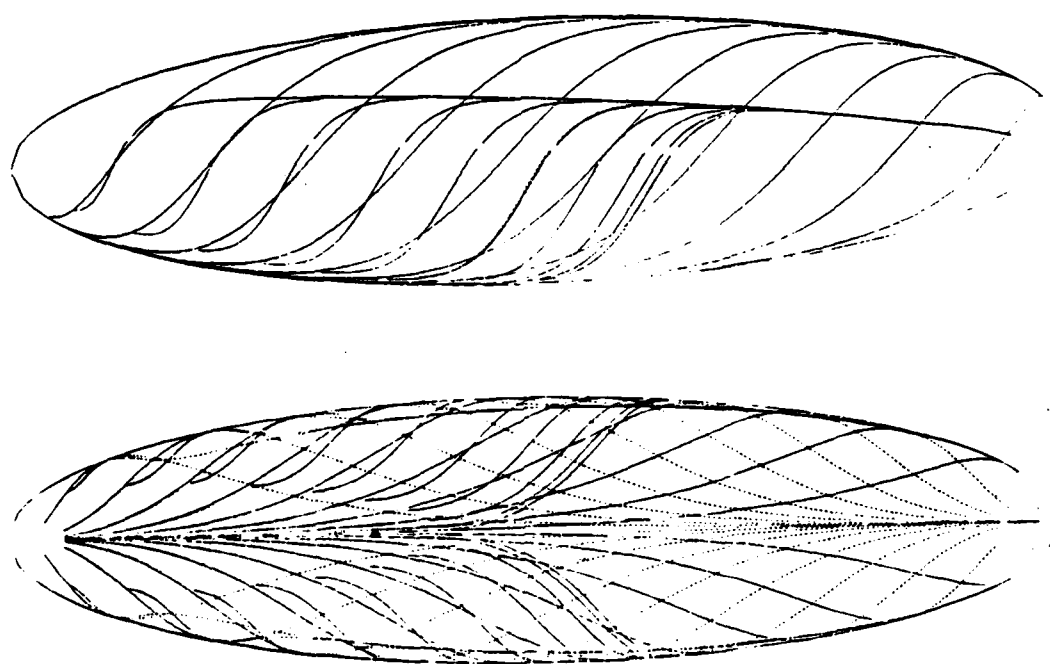


Fig. 2 Flow about an ellipsoid with axes ratios $a:b:c = 4:1:1$ (prolate spheroid) at an angle of attack $\alpha = 30^\circ$.

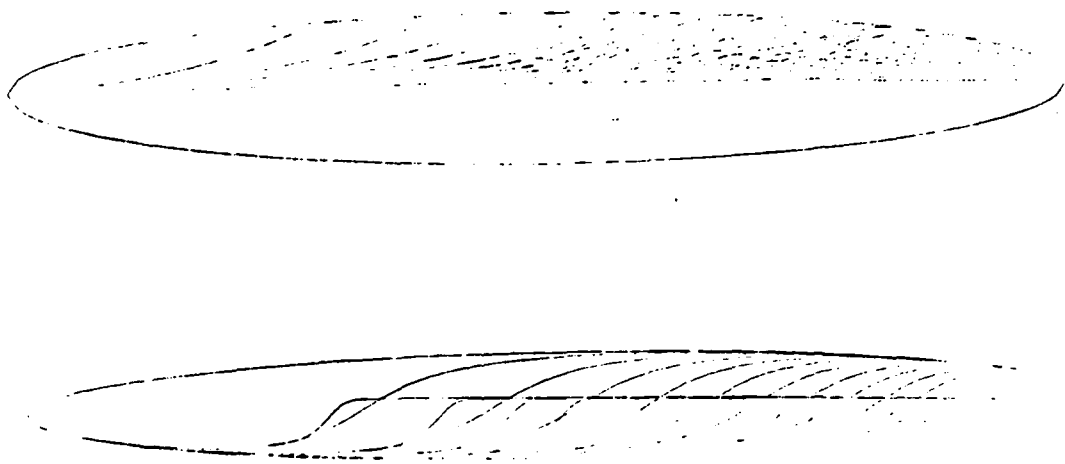


Fig. 3 Flow about an ellipsoid with axes ratios $a:b:c = 70:10:7$ and a free stream $U_\infty = \cos 15^\circ$, $V_\infty = \sin 15^\circ$, $W_\infty = \sin 15^\circ$.

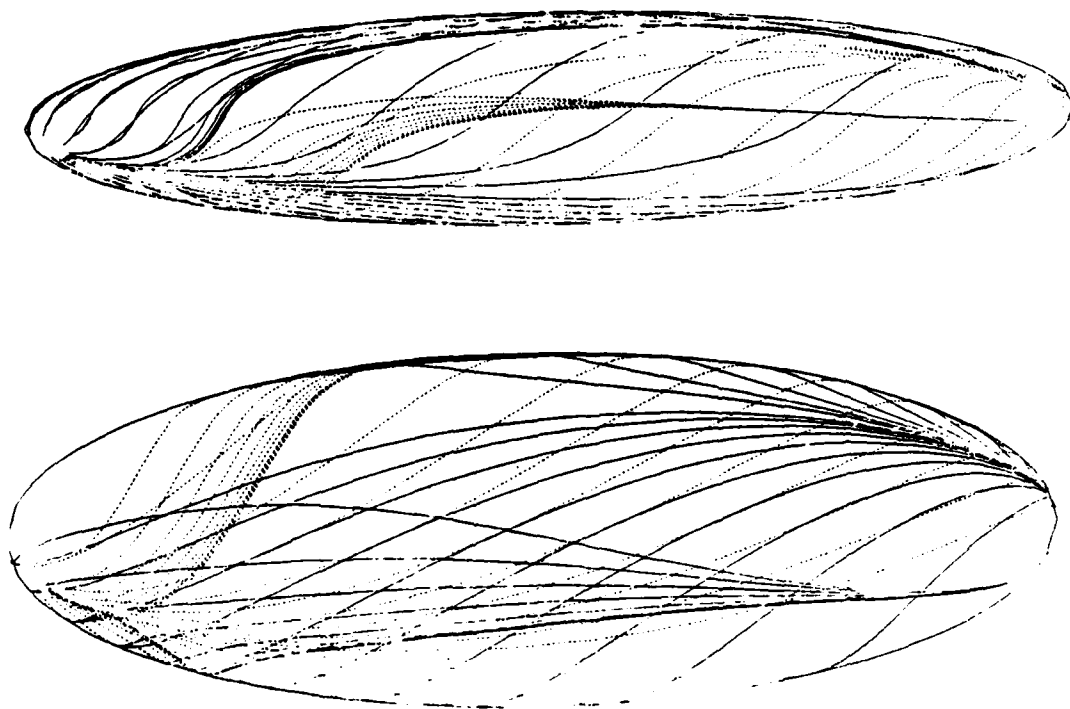


Fig. 4 Flow about an ellipsoid with axes ratios $a:b:c = 50:30:10$ and free stream $U_\infty = \cos 30^\circ$, $V_\infty = \sin 15^\circ$, $W_\infty = \sin 15^\circ$.

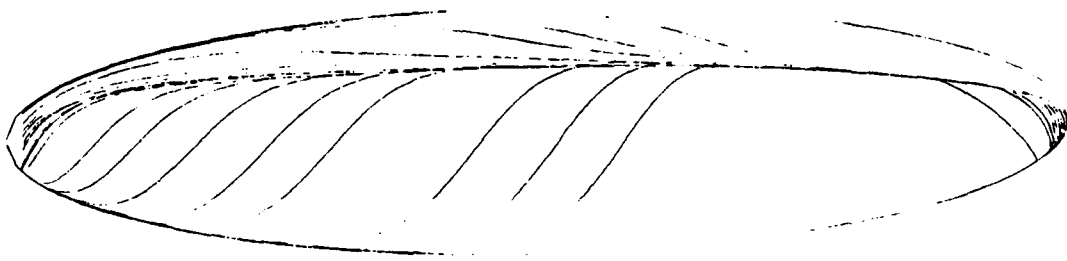


Fig. 5 Flow about an ellipsoid with axes ratios $a:b:c = 4:1:1$ (prolate spheroid) at an angle of attack $\alpha = 30^\circ$ (surface-streamline integration method).

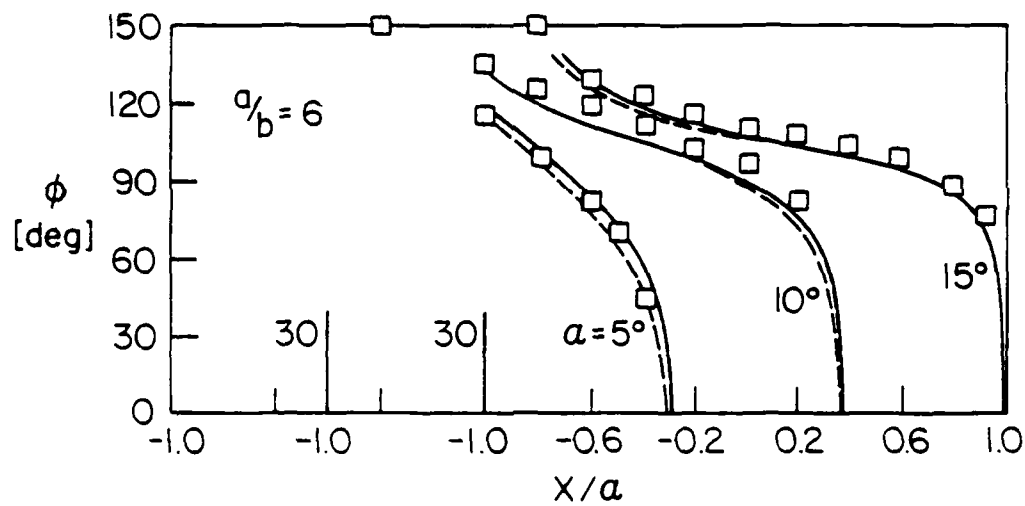


Fig. 6 Lines of separation for a prolate spheroid with axes ratios $a/b = 6$ and angles of attack $\alpha = 5^\circ, 10^\circ$ and 15° . —, Stock⁸, ----, Geissler¹⁹; \square , present method.

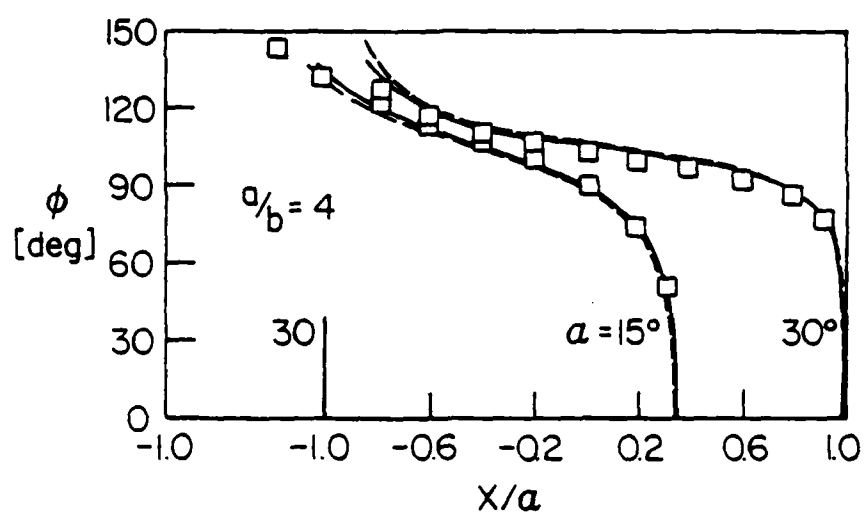


Fig. 7 Lines of separation for a prolate spheroid with axes ratios $a/b = 4$ and angles of attack $\alpha = 15^\circ$ and 30° . —, Stock⁸; ----, Geissler¹⁹; \square , present method.

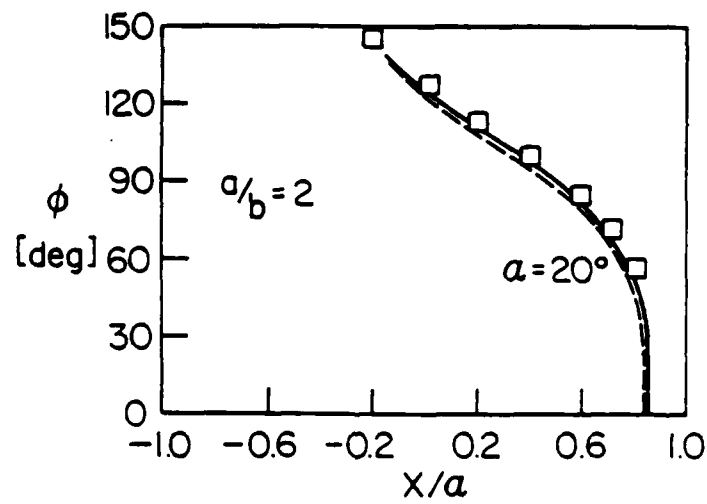


Fig. 8 Lines of separation for a prolate spheroid with axes ratios $a/b = 2$ and angle of attack $\alpha = 20^\circ$. —, Stock⁸; ----, Geissler¹⁹; \square , present method.

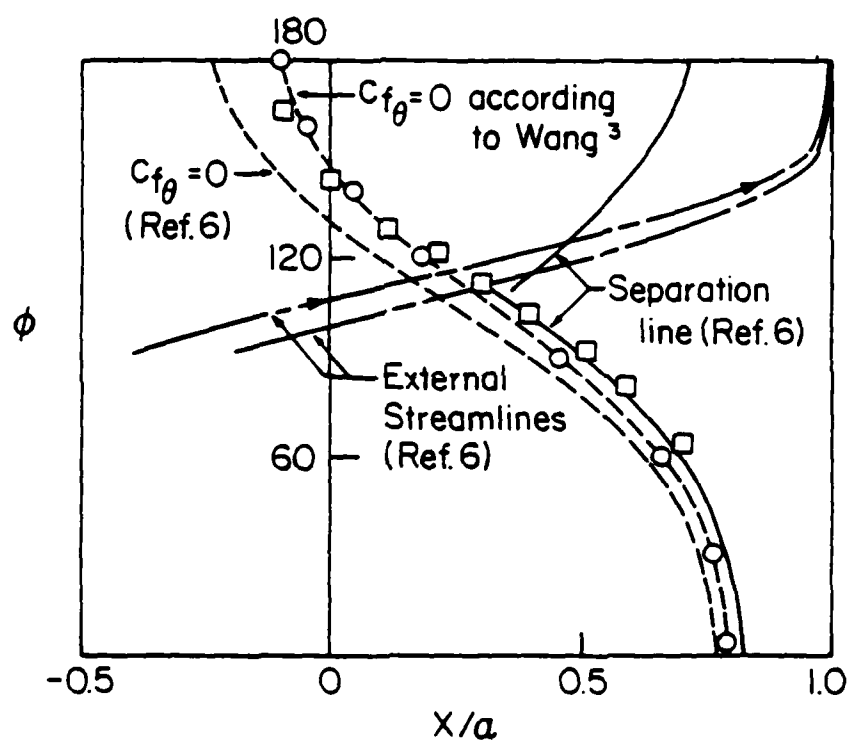


Fig. 9 Lines of separation and external streamlines for a prolate spheroid of $\alpha/b = 6$ at an angle of attack $\alpha = 6^\circ$. —, Ref. 6; ----, Ref. 3; \square , present approximate method.

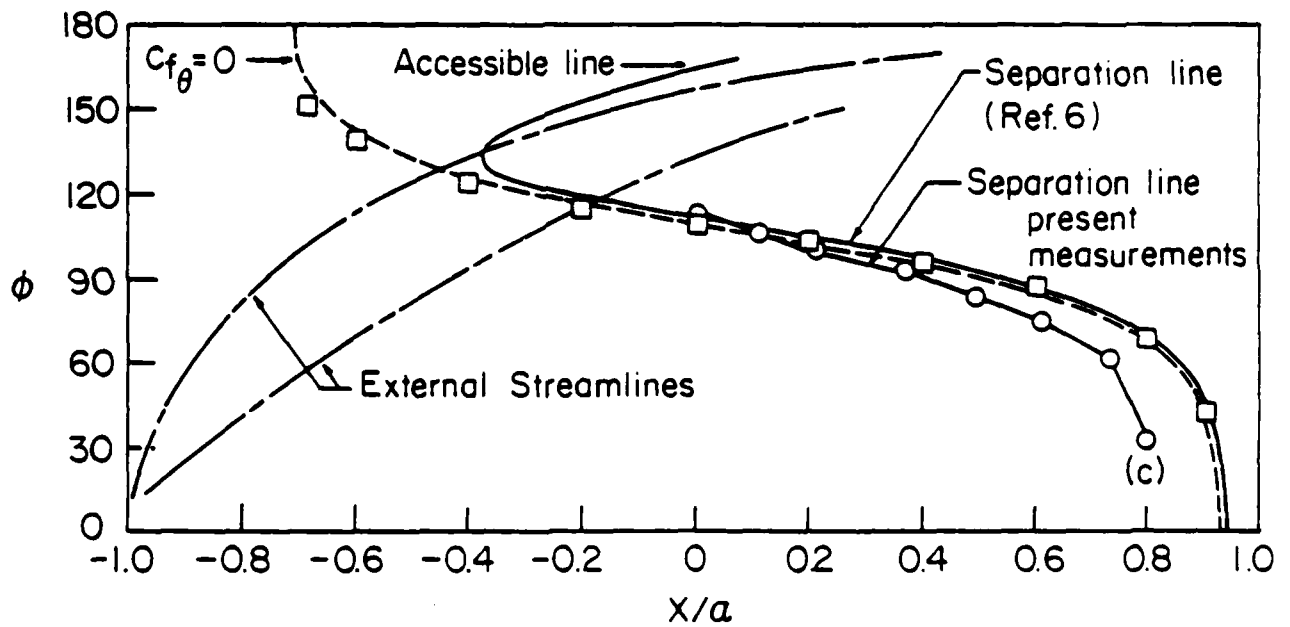


Fig. 10 Lines of separation and external streamlines for a prolate spheroid of $a/b = 6$ at an angle of attack $\alpha = 15^\circ$ as reported in Ref. 6; \square , present approximate method; $-o-o-o-o-$, present experimental data.

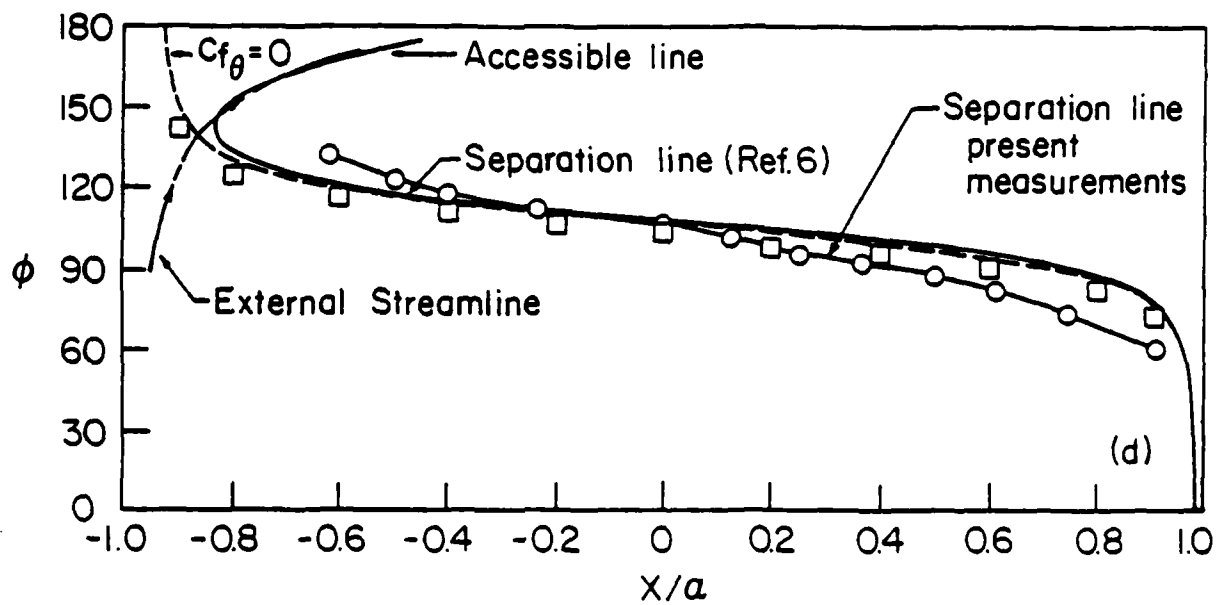
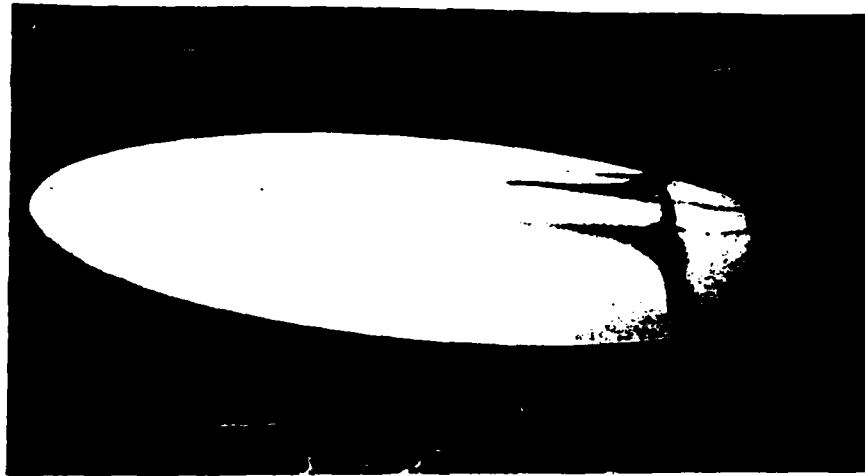


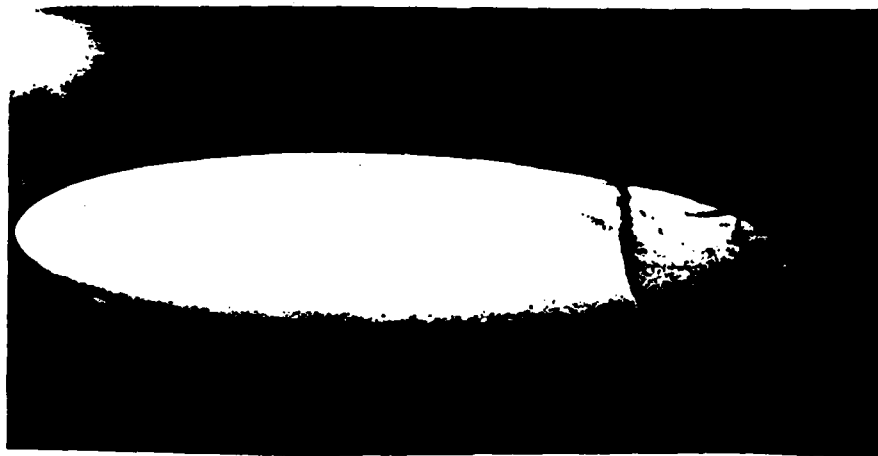
Fig. 11 Lines of separation and external streamlines for a prolate spheroid of $a/b = 4$ at an angle of attack $\alpha = 30^\circ$ as reported in Ref. 6; \square , present approximate method; o-o-o-o-o; present experimental data.



(a)

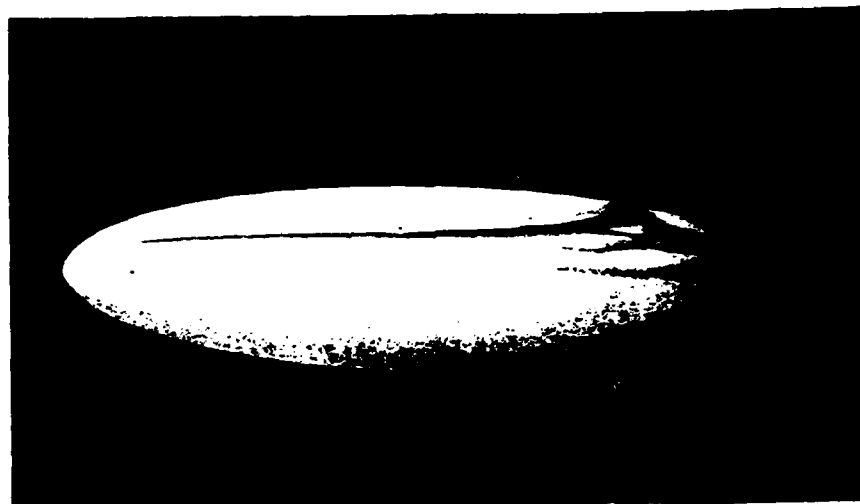


(b)



(c)

Fig. 12 Skin friction lines for $\alpha = 3^\circ$. (a) Leeward view, (b) View from $\phi = 120^\circ$, (c) Side view.



(a)

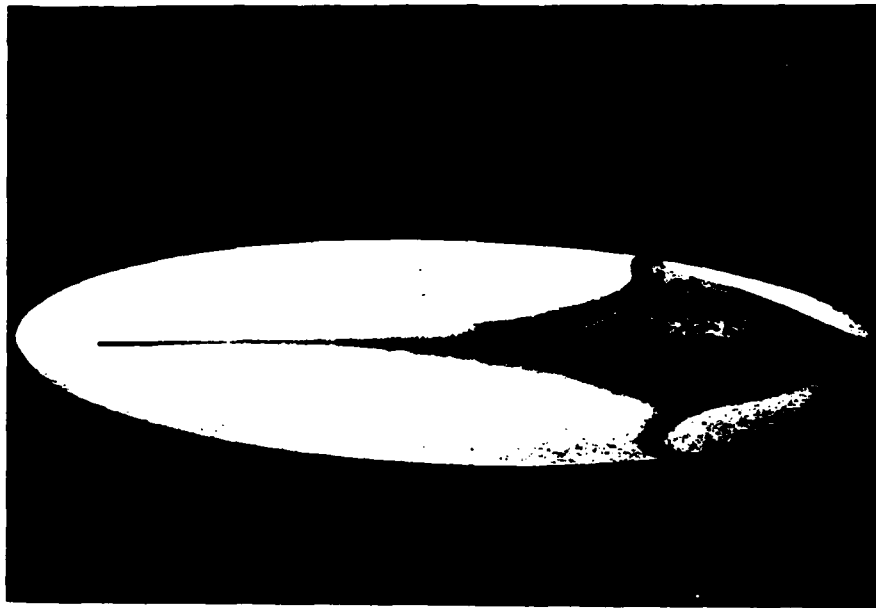


(b)

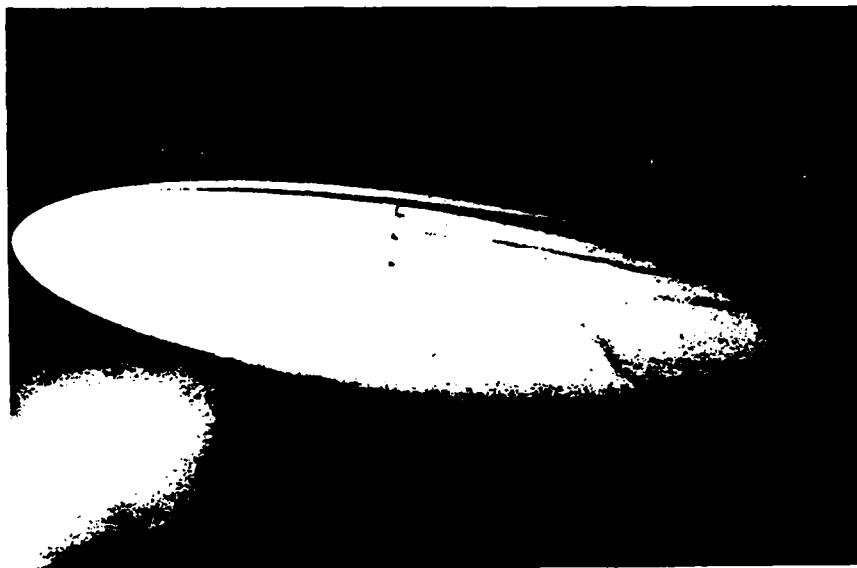


(c)

Fig. 13 Skin friction lines for $\alpha = 6^\circ$. (a) Leeward view, (b) View from $\phi = 120^\circ$, (c) Side view.



(a)



(b)

Fig. 14. Skin friction and inviscid lines for $\alpha = 10^\circ$. (a) Leeward view; (b) View from $\phi = 120^\circ$.



(a)



(b)

Fig. 15 Skin friction and inviscid lines for $\alpha = 20^\circ$. (a) Leeward view, (b) View from $\phi = 120^\circ$.

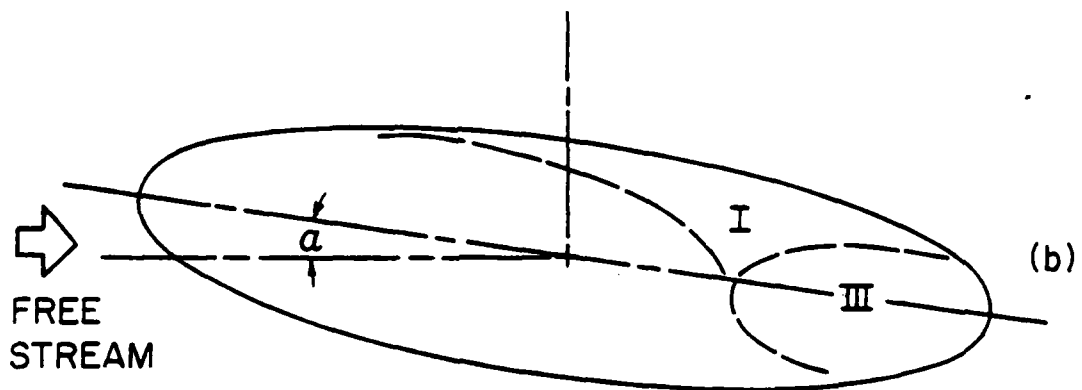
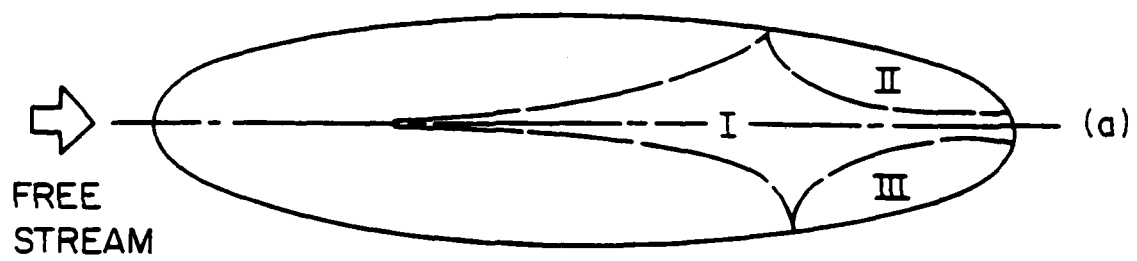


Fig. 16 The three regions of difficult accessibility for $\alpha = 10^\circ$.
 (a) Leeward view, (b) View from $\phi = 120^\circ$.



(a)



(b)

Fig. 12 Skin friction and inviscid lines for $\alpha = 30^\circ$. (a) Leeward view, (b) View from $\phi = 120^\circ$.

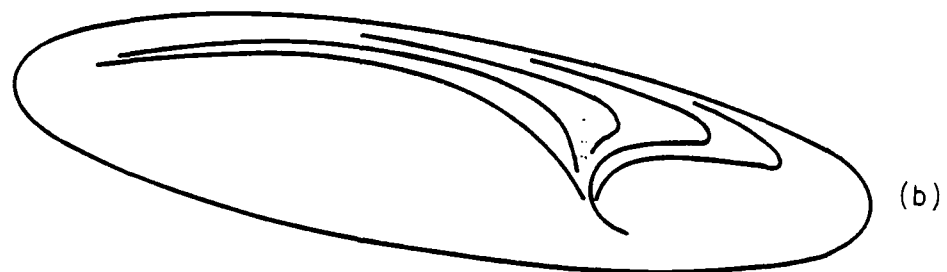
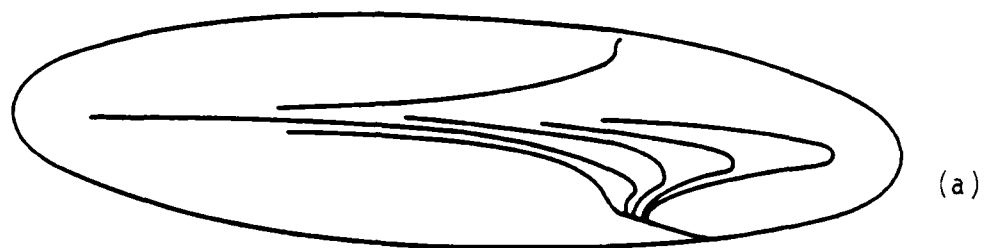


Fig. 18 Approximate form of skin friction lines for $\alpha = 10^\circ$.
(a) Leeward view, (b) View from $\phi = 120^\circ$.

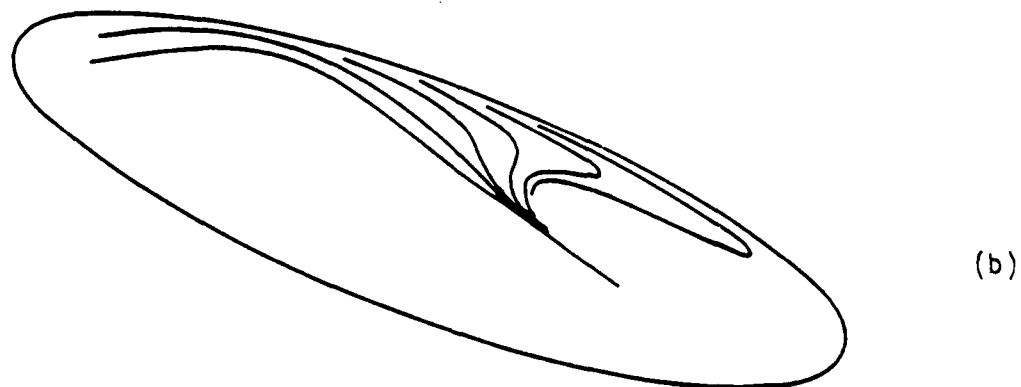
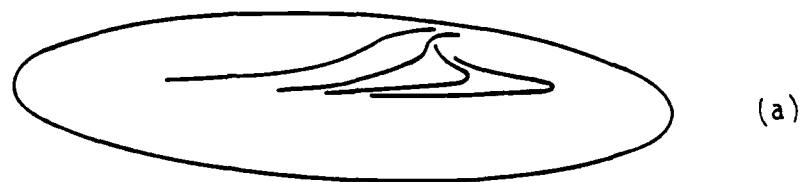


Fig. 19 Approximate form of skin friction lines for $\alpha = 20^\circ$.
(a) Leeward view, (b) View from $\phi = 120^\circ$.

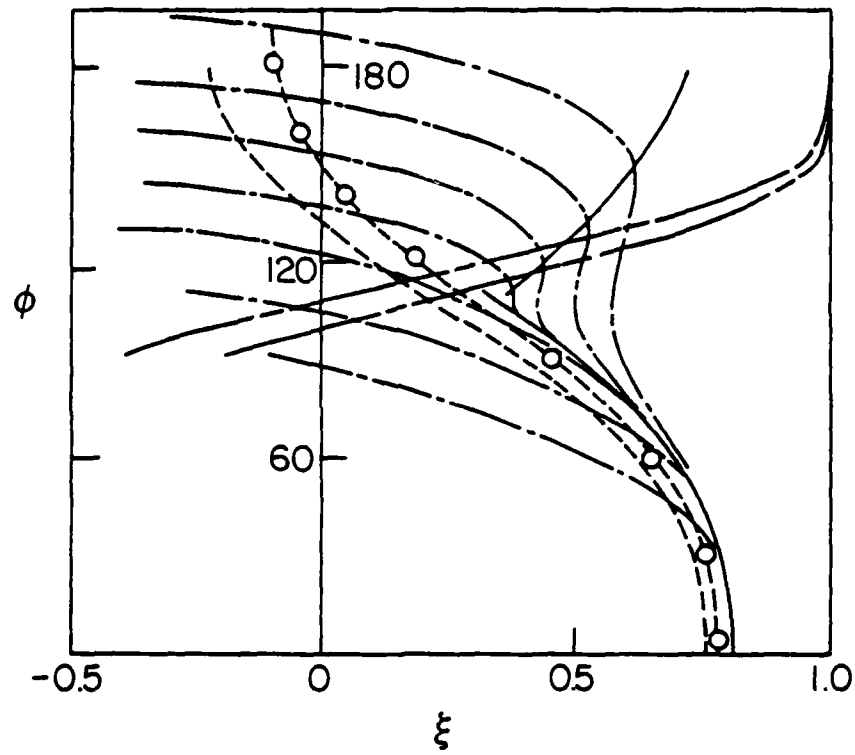


Fig. 20 Qualitative shape of skin-friction lines superimposed on a Figure from Ref. 6.

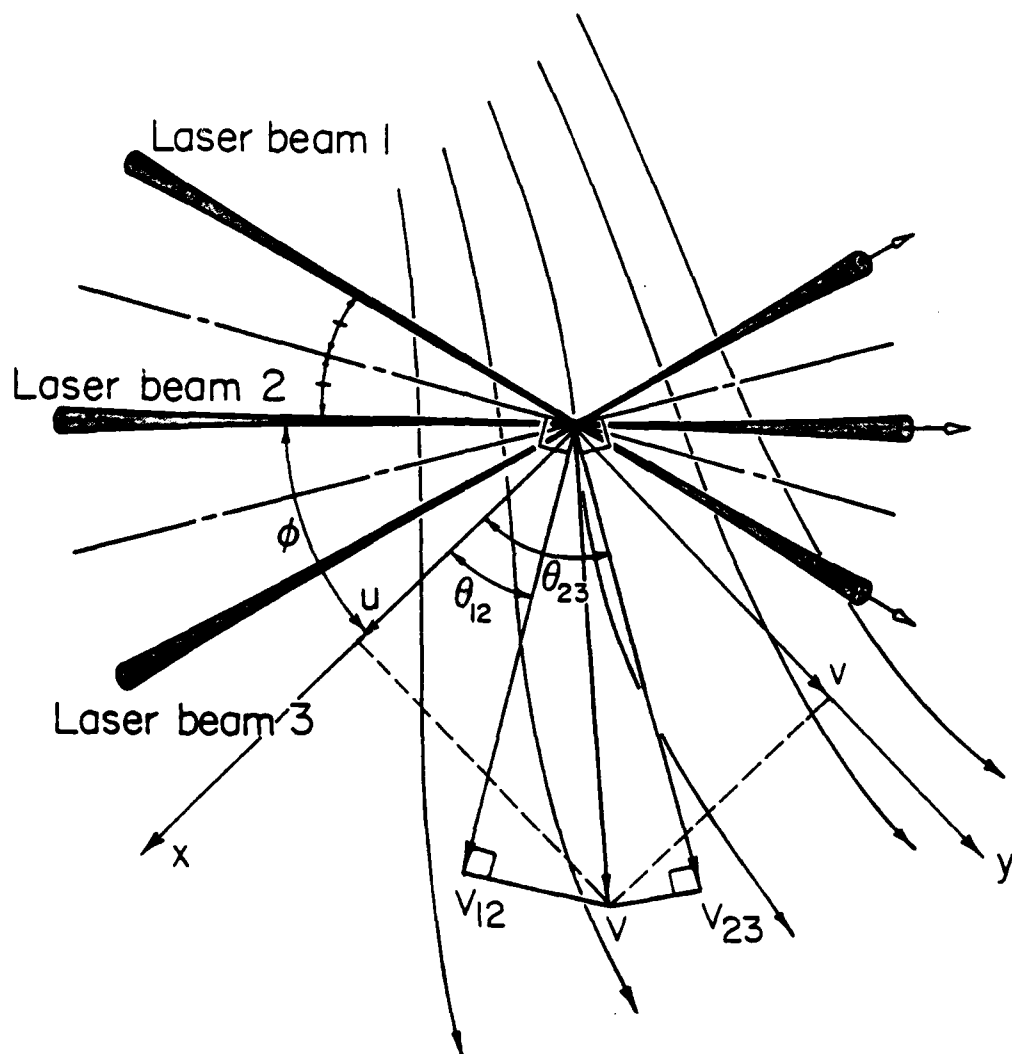


Fig.21 Schematic representation of the crossing of 3 beams. All 3 beams are in the same plane. Interference between beam 1 and 2 generates the velocity component V_{12} and interference between 2 and 3 generates the component V_{23} .

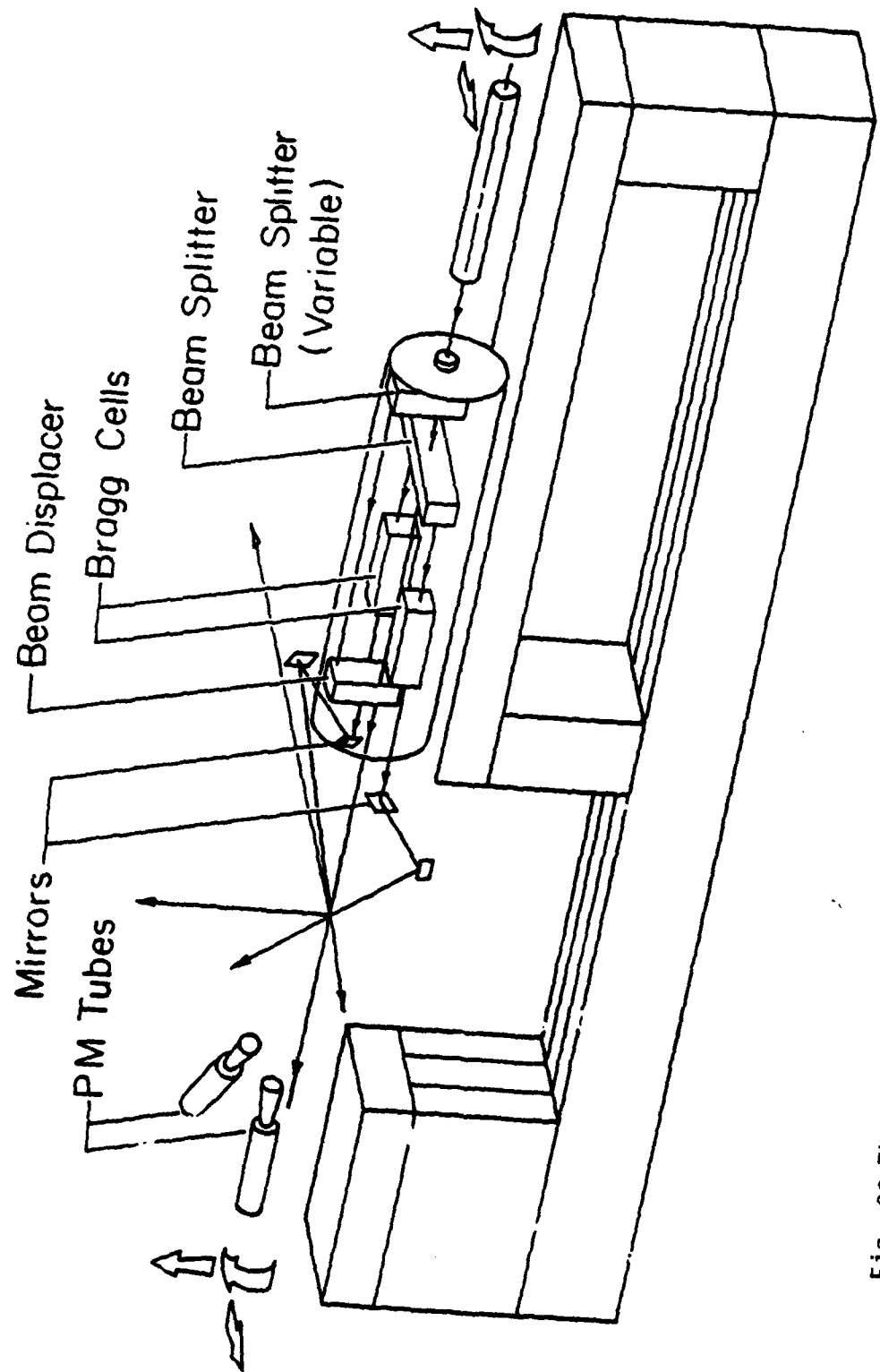


Fig. 22 The optical bench for the measurement of 2 components.

TYPE TRON25 RESULT

START OF TARE
MODE:OPTION1.C

A1 DIST IS 1-2= 15.379 **1-3= 15.202
 A1 DIST IS 1-2= 28.855 **1-3= 29.826
 0.1138 0.1326 0.0644 0.1419 0.1132
 ANGLES OF INCLIN TRANSU ARE:
 0.0069 0.0172 -0.0069 0.0057
 *ANGLES OF MEASUREMENT ARE:
 3.65012 -2.46812
 ANGLES OF MEASUR VELOC :
 F1 = 6.392 F2 = 4.775

***THFFF= 14.999987

CARTESIAN X-COORDINATE OF THE MEASUREMENT X= 0.25

ANGLE OF THE POINT OF THE MEASUREMENT IN DEG FHI= 90.00

INCLINATION OF THE BEAMS W.R.TO THE DIRECTION OF FLOW TH1= 6.484

INCLINATION OF BEAMS W.R.TO THE HORIZONTAL
 THE F
 LOW TH2 =
 0.329

WALL AND TRANSVERSE TO

R; T=0.04/0.13 02:29:31

OPTION75B/5.02 02:28:32

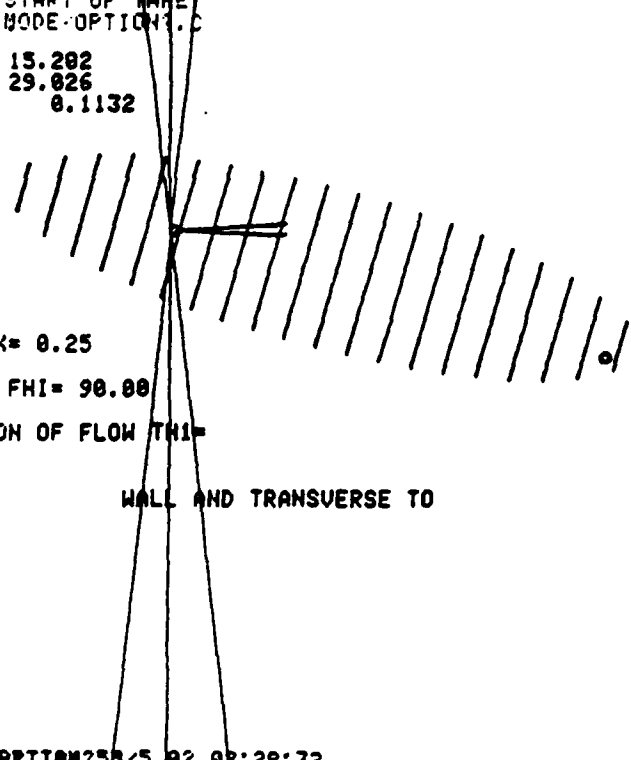


Fig. 23 Example of laser beam locations with respect to the body and output of program for the calculation of measuring position.

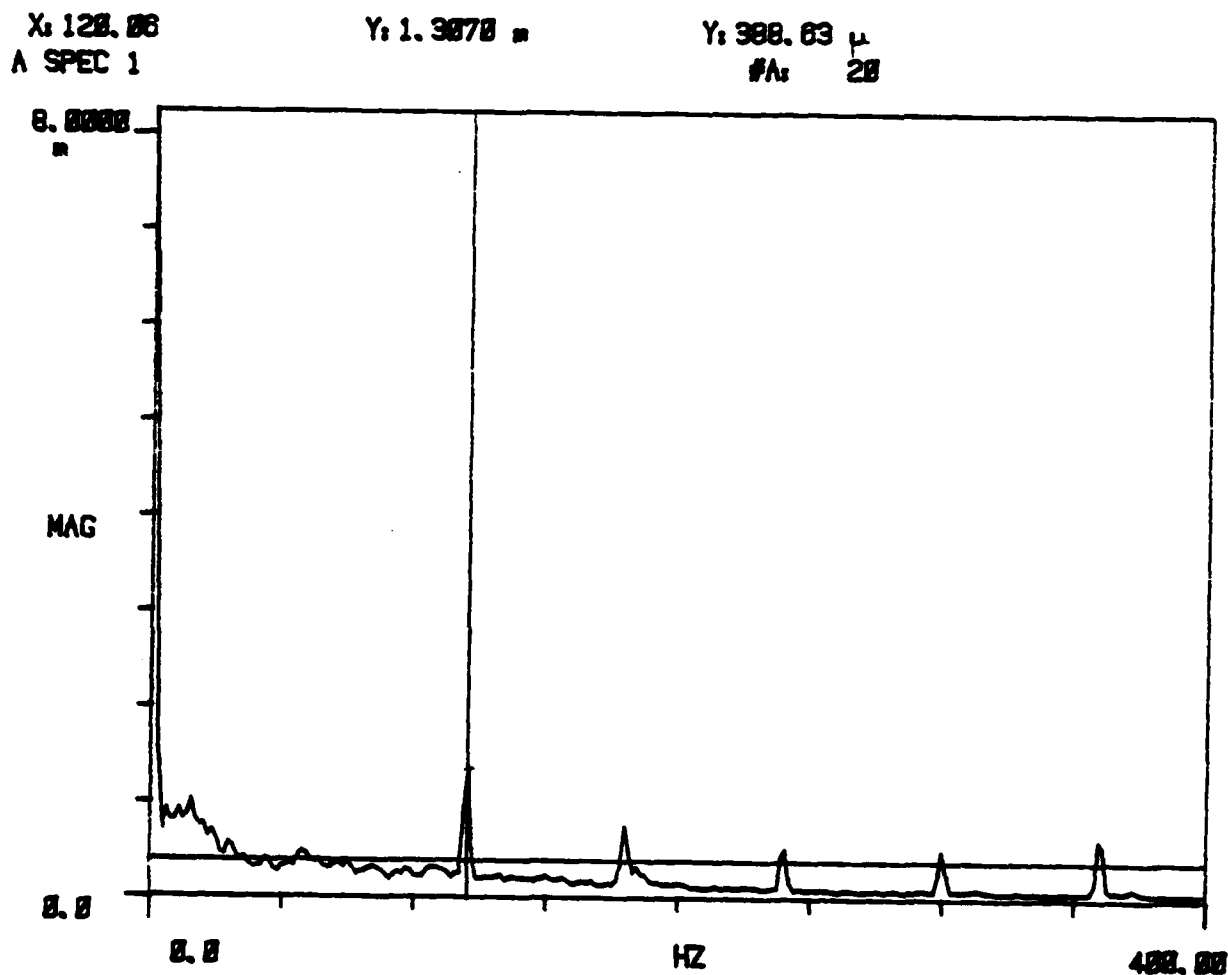


Fig. 25 RMS spectrum of the velocity fluctuation. If the low frequencies (less than 1 Hz) are eliminated, then the turbulence level is less than 0.1%. The spikes in the spectrum correspond to the 60 Hz and its multiples and are due to the power supply.

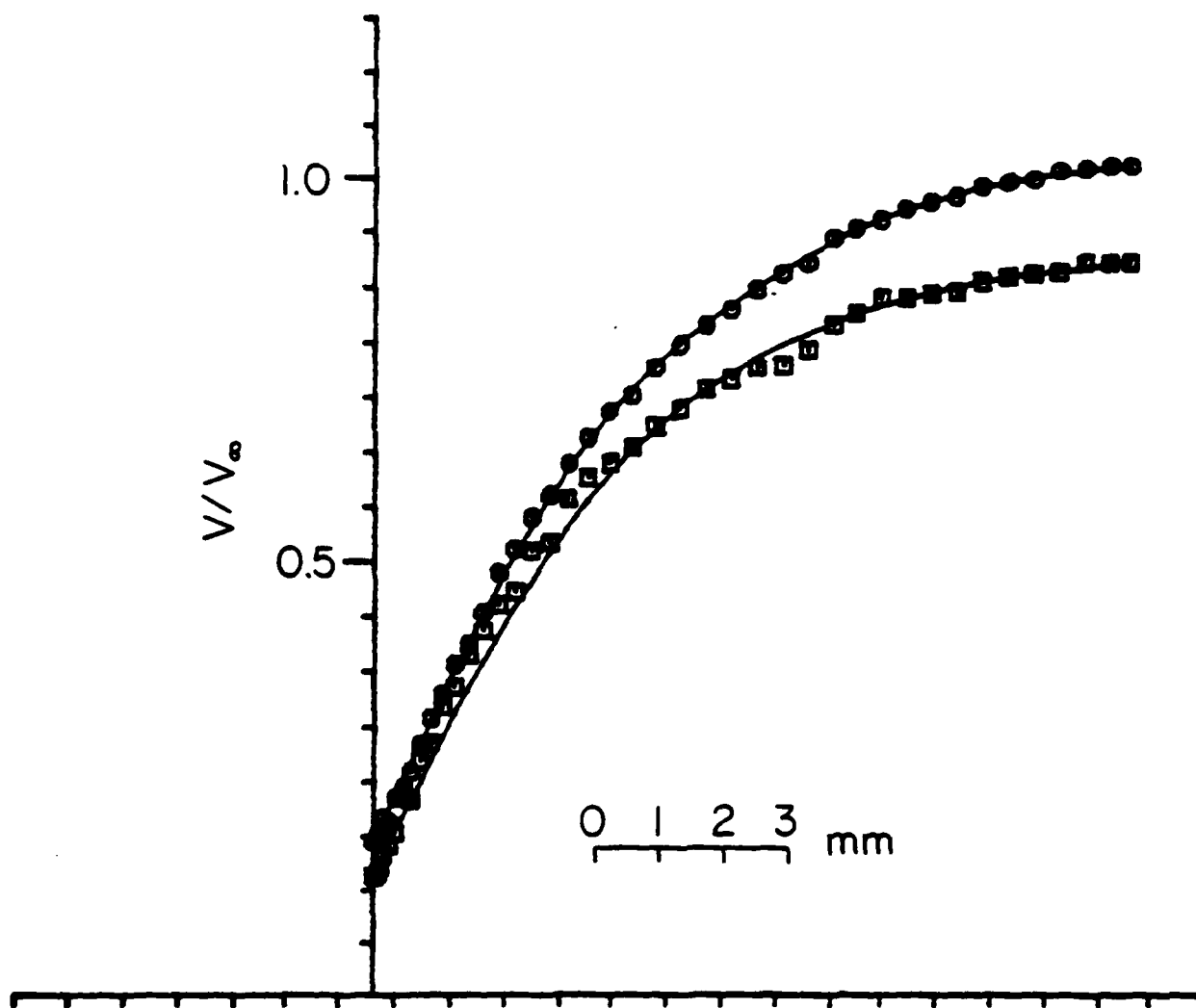


Fig. 26 The actual experimental points shown together with the smoothed profile on the leeward side at the fourth station.

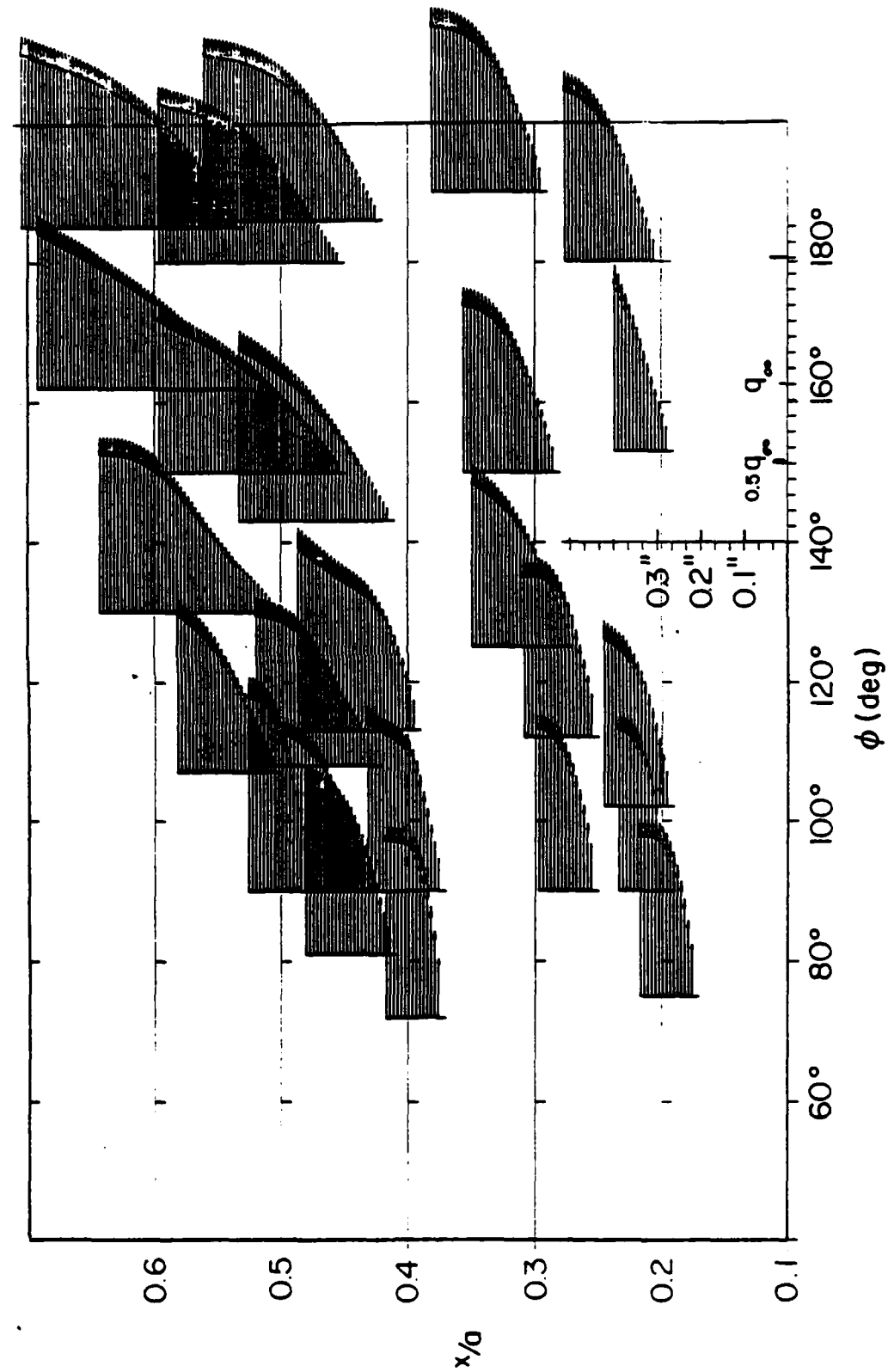


Fig. 27. The u-component velocity profile. Horizontal and vertical scales are marked in tenths of free steam velocity and increments of 1/10" (and 0.85 mm) respectively.

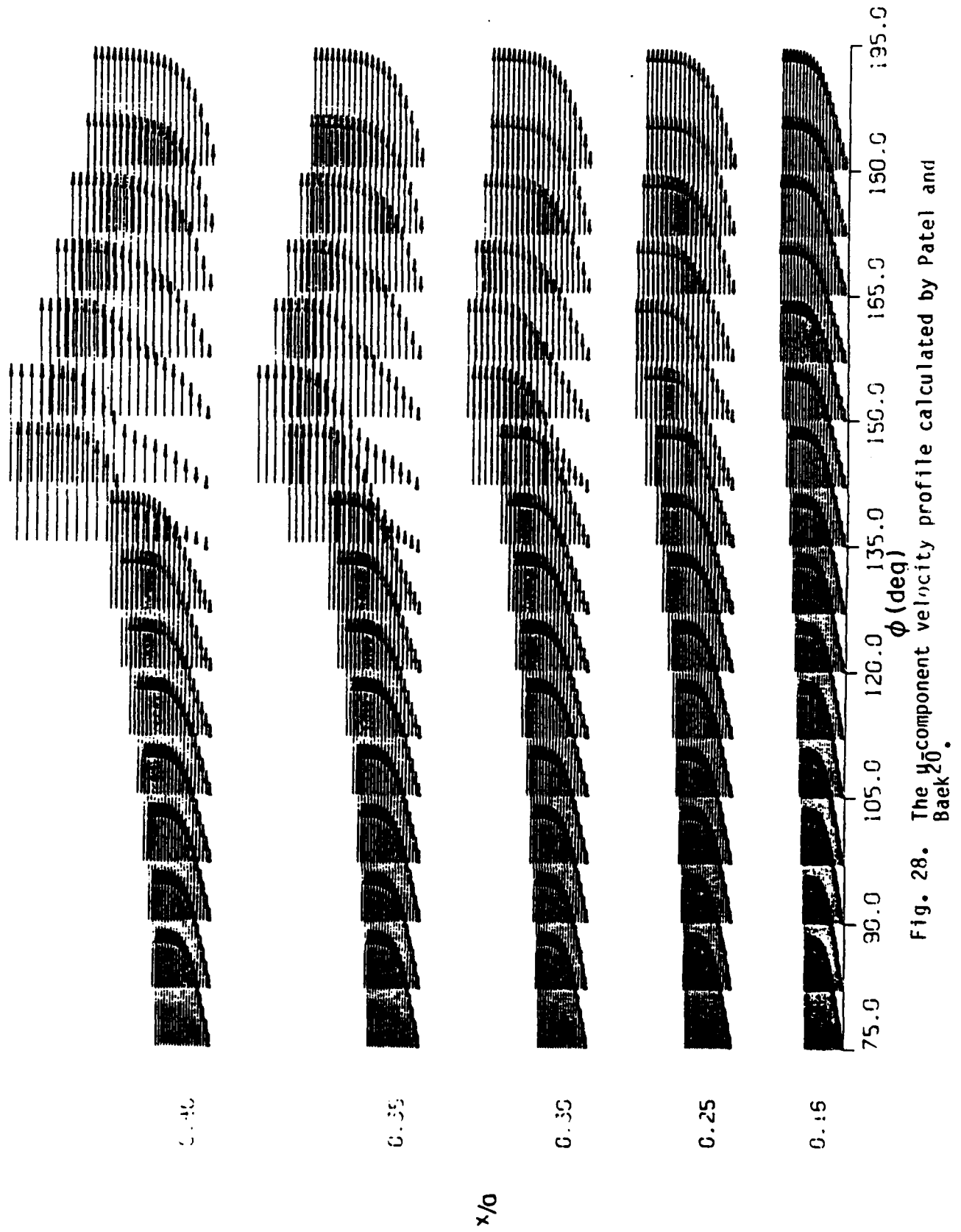


Fig. 28. The u -component velocity profile calculated by Patel and Baek²⁰.

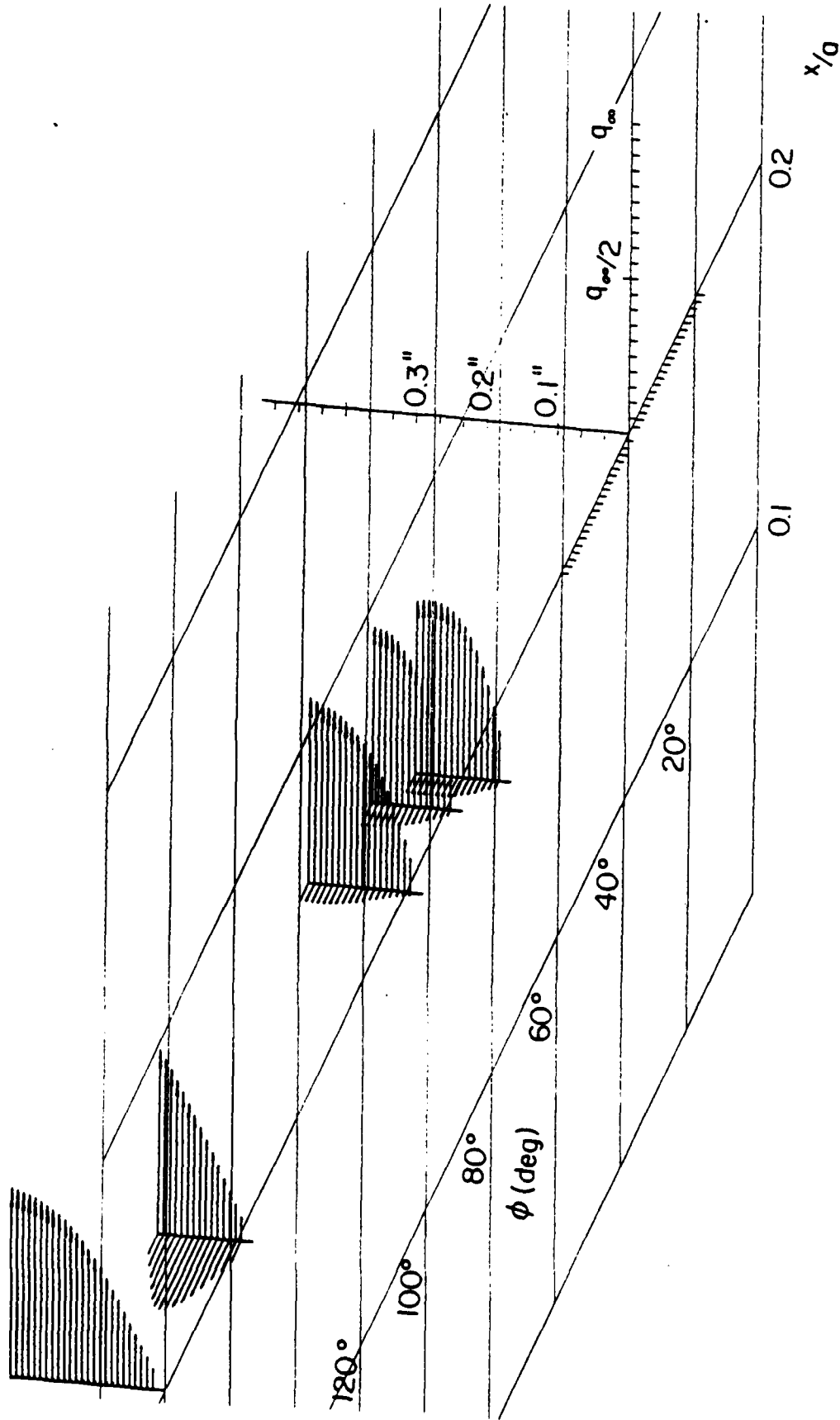


Fig. 29. The u- and v-velocity components at the first station of measurement.

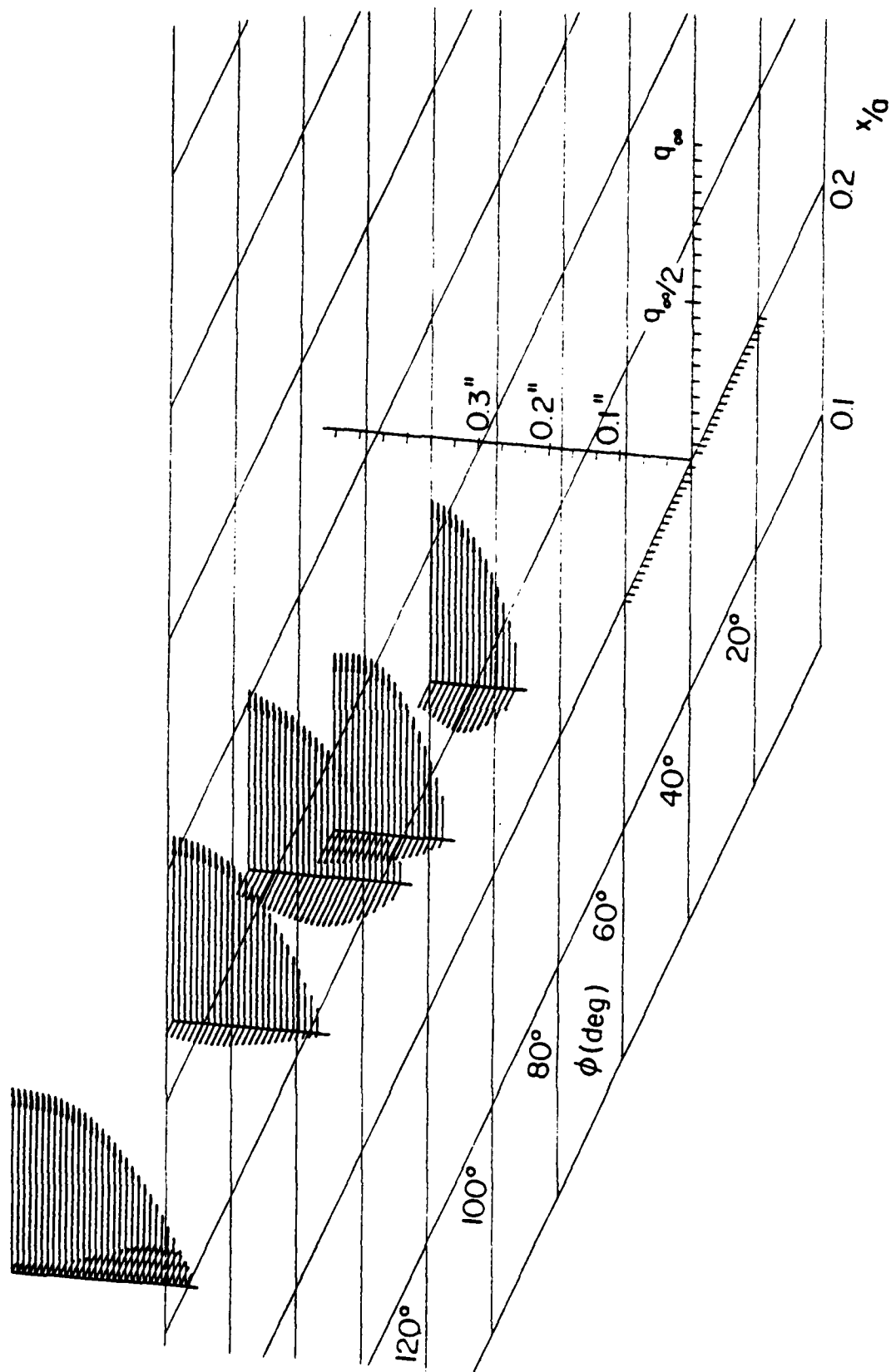


Fig. 30. The u - and v -velocity components at the second station of measurement.

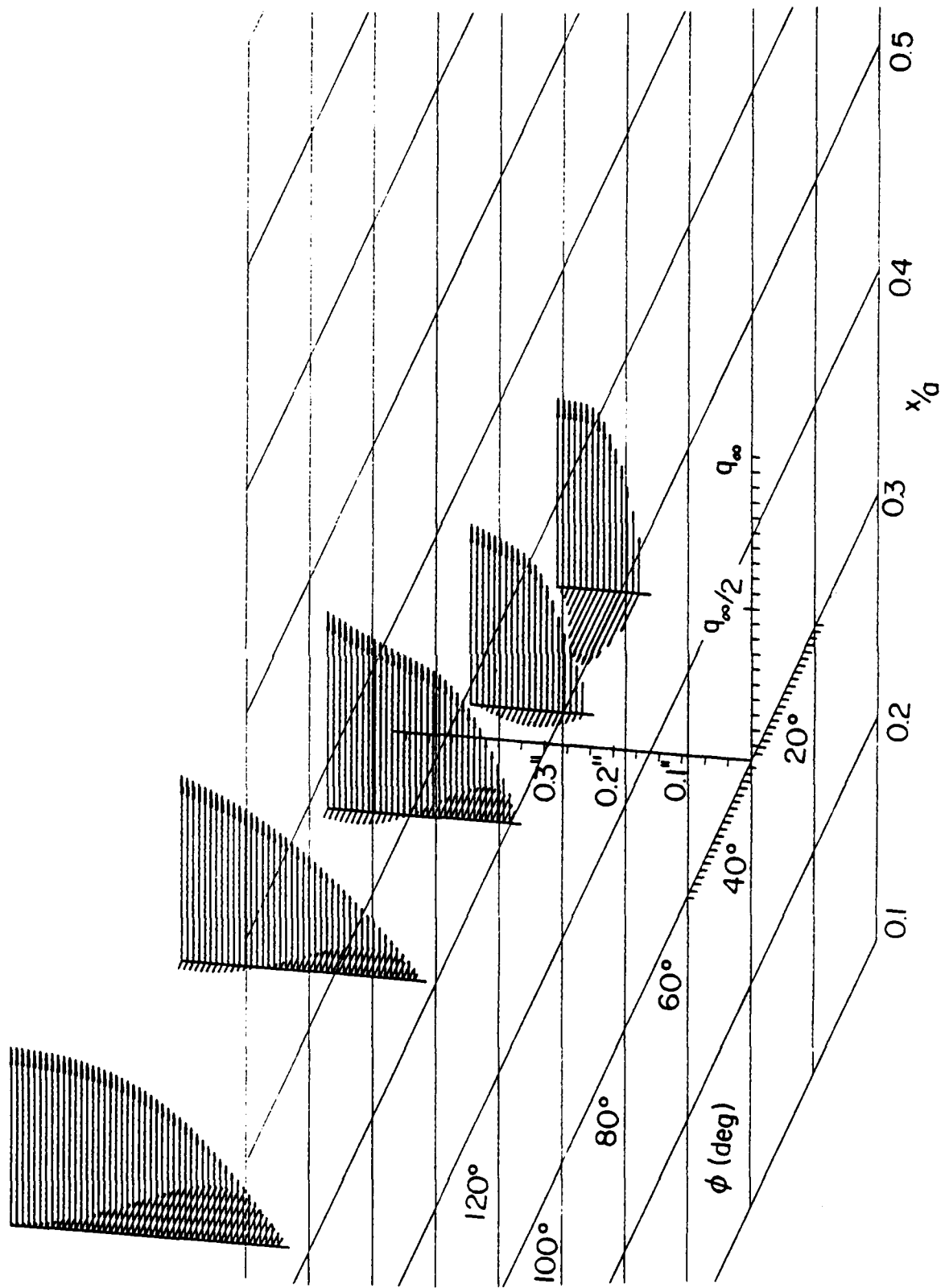


Fig. 31. The u - and v -velocity components at the third station of measurement.

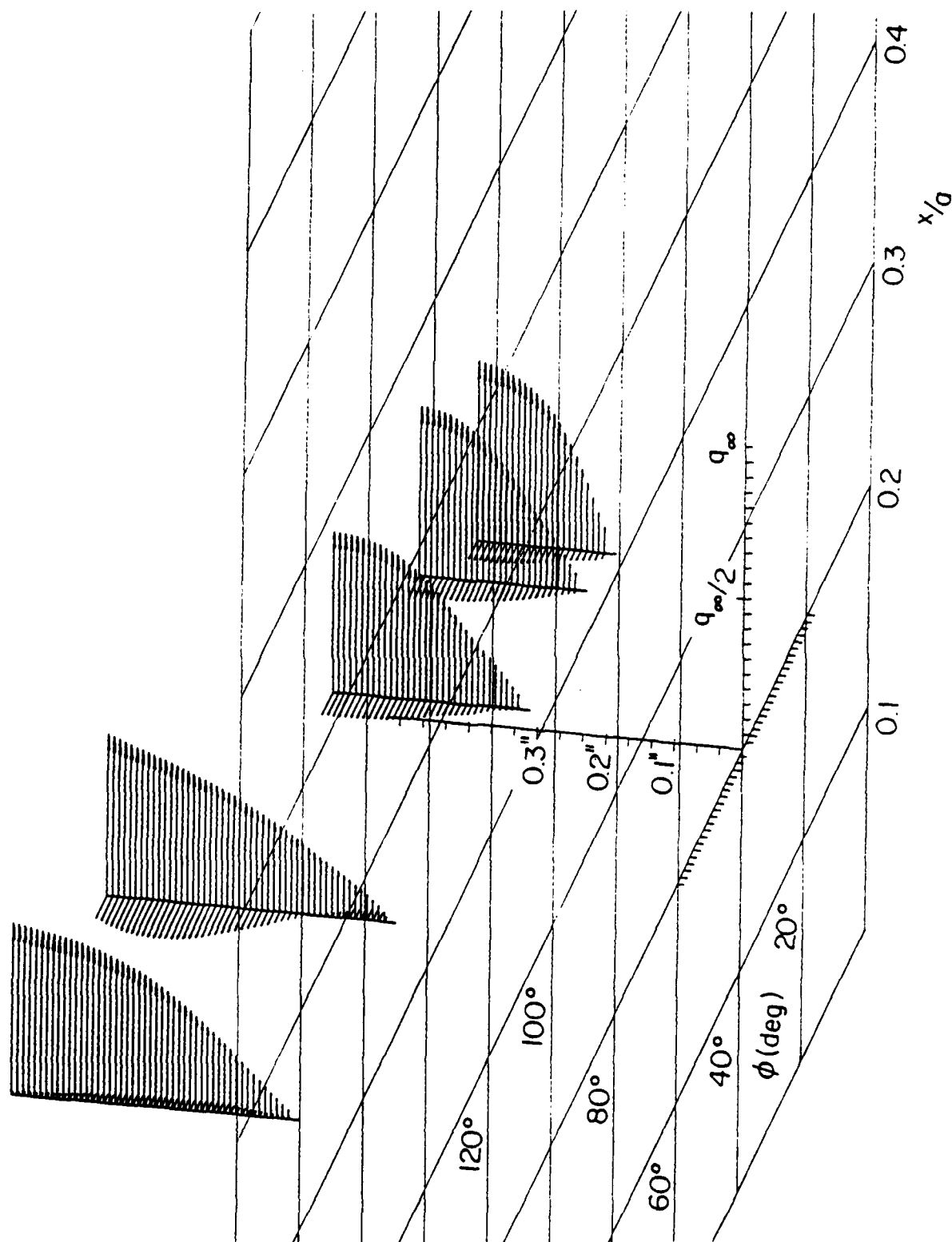


Fig. 32. The u - and v -velocity components at the fourth station of measurement.

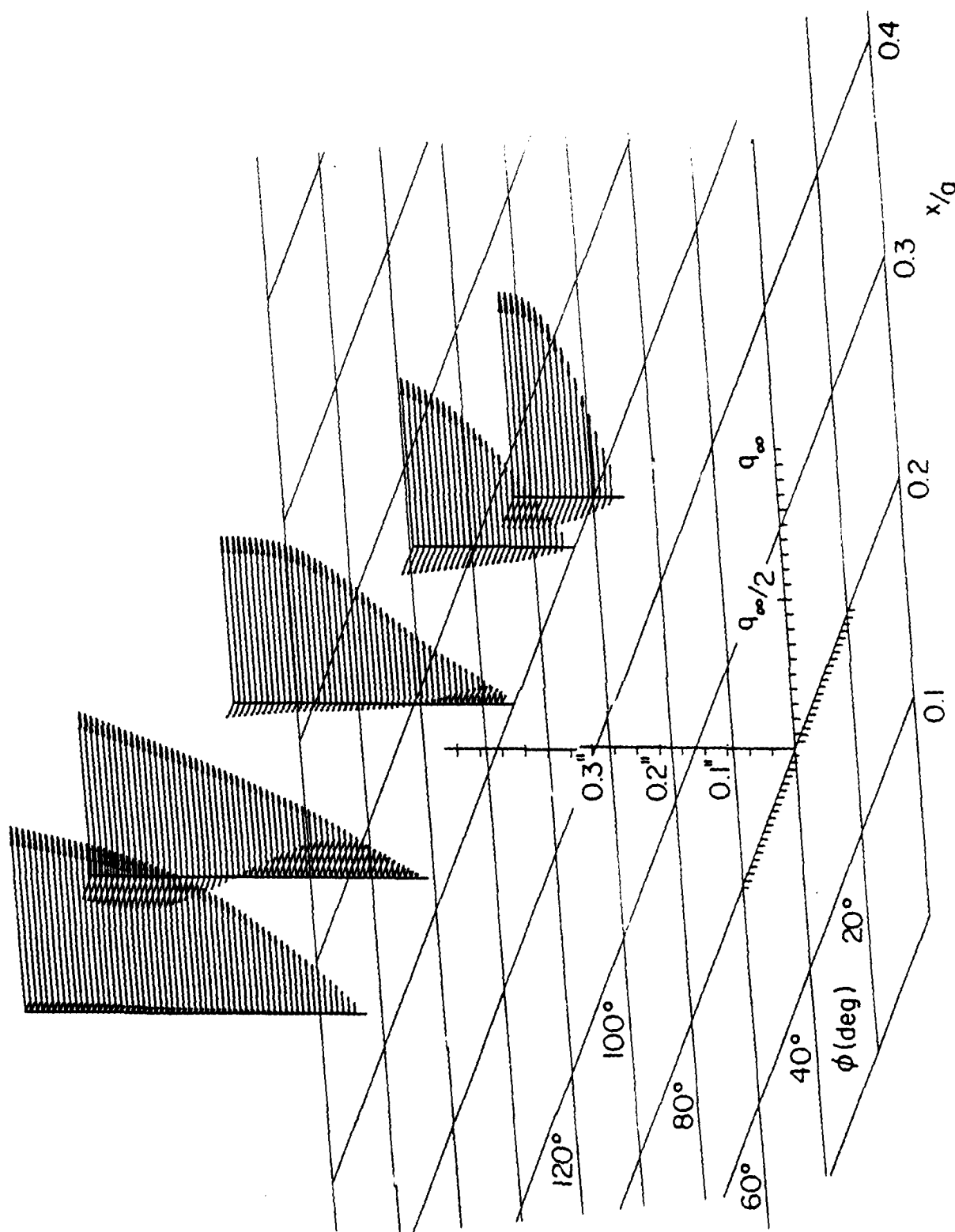


Fig. 33. The u - and v -velocity components at the fifth station of measurement.

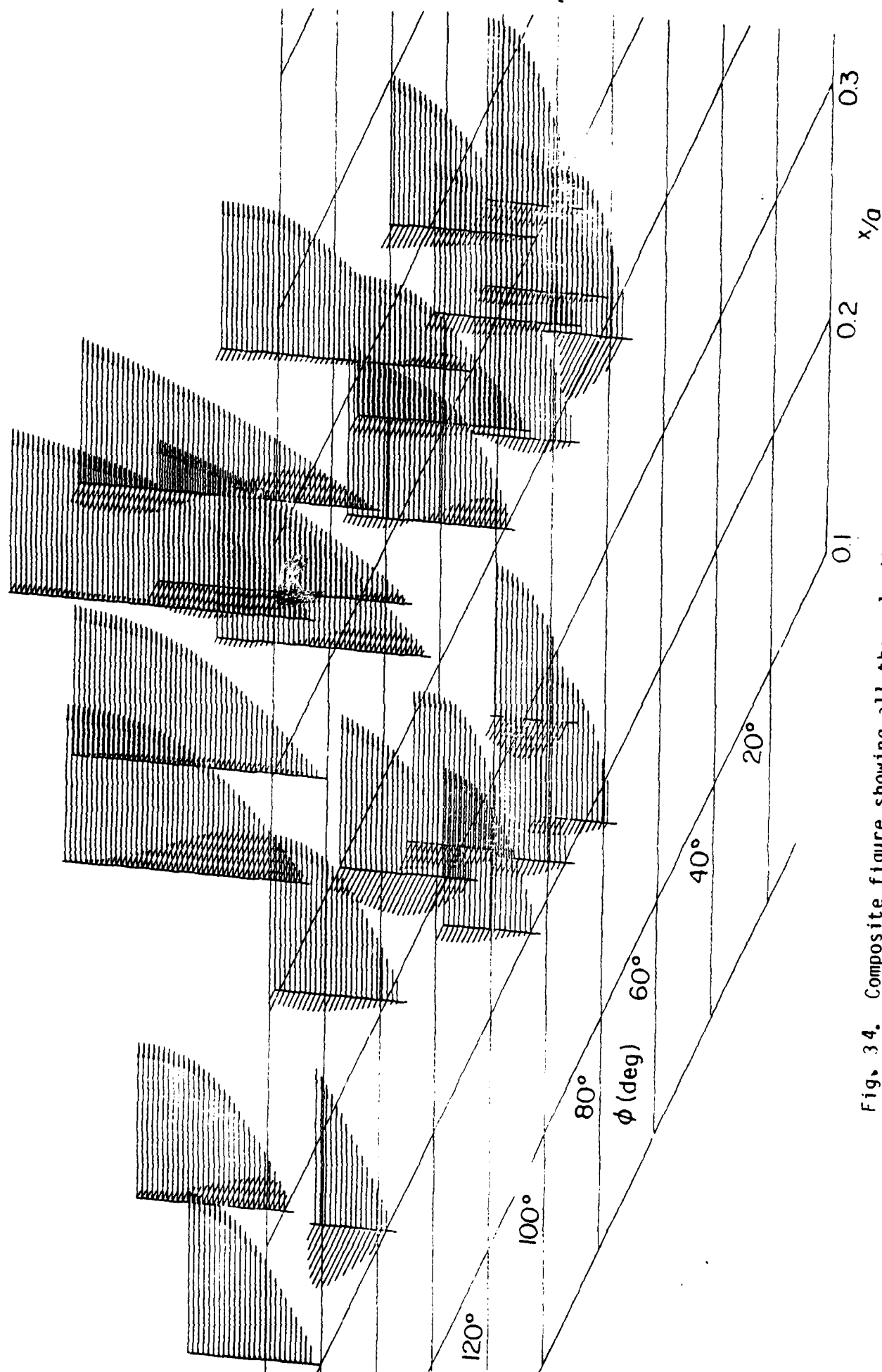


Fig. 34. Composite figure showing all the velocity profiles in the two-dimensional space of the ellipsoid surface.

END

FILMED

6-34

DTIC